2016

A carbon budget for the Amundsen Sea Polynya, Antarctica: Estimating net community production and export in a highly productive polar ecosystem

PL Yager

RM Sherrell

et al

RE Sipler
Virginia Institute of Marine Science

et al

ELEMENTA
Science of the Anthropocene

A carbon budget for the Amundsen Sea Polynya, Antarctica: Estimating net community production and export in a highly productive polar ecosystem

PL Yager[1*] • RM Sherrell[2] • SE Stammerjohn[3] • HW Ducklow[4] • OME Schofield[2] • ED Ingall[5] • SE Wilson[6] • KE Lowry[7] • CM Williams[1] • L Riemann[8] • S Bertilsson[9] • A-C Alderkamp[7] • J Dinasquet[8,10] • R Logares[11] • I. Richert[9] • RE Sipler[12] • AJ Melara[1] • L Mu[1] • RG Newstead[6] • AF Post[13] • R Swalethorp[14,15] • GL van Dijken[7]

[1]Department of Marine Sciences, University of Georgia, Athens, Georgia, United States
[2]Department of Marine and Coastal Sciences, Rutgers University, New Brunswick, New Jersey, United States
[3]Institute of Arctic and Alpine Research, University of Colorado, Boulder, Colorado, United States
[4]Lamont-Doherty Earth Observatory, Columbia University, Palisades, New York, United States
[5]School of Earth and Atmospheric Sciences, Georgia Institute of Technology, Atlanta, Georgia, United States
[6]School of Ocean Sciences, Bangor University, Bangor, Gwynedd, United Kingdom
[7]Department of Earth System Science, Stanford University, Stanford, California, United States
[8]Marine Biological Section, University of Copenhagen, Helsingør, Denmark
[9]Department of Ecology and Genetics, Limnology and Science for Life Laboratory, Uppsala University, Uppsala, Sweden
[10]Department of Natural Sciences, Linnaeus University, Kalmar, Sweden
[11]Institute of Marine Sciences, CSIC, Barcelona, Spain
[12]Virginia Institute of Marine Science, College of William & Mary, Gloucester Pt., Virginia, United States
[13]Harbor Branch Oceanographic Institute, Florida Atlantic University, Boca Raton, Florida, United States
[14]National Institute of Aquatic Resources (DTU Aqua), Section for Oceanography and Climate, Technical University of Denmark, Charlottenlund, Denmark
[15]Department of Biology and Environmental Sciences, University of Gothenburg, Göteborg, Sweden

*pyager@uga.edu

Abstract

Polynyas, or recurring areas of seasonally open water surrounded by sea ice, are foci for energy and material transfer between the atmosphere and the polar ocean. They are also climate sensitive, with both sea ice extent and glacial melt influencing their productivity. The Amundsen Sea Polynya (ASP) is the greenest polynya in the Southern Ocean, with summertime chlorophyll *a* concentrations exceeding 20 μg L^{-1}. During the Amundsen Sea Polynya International Research Expedition (ASPIRE) in austral summer 2010–11, we aimed to determine the fate of this high algal productivity. We collected water column profiles for total dissolved inorganic carbon (DIC) and nutrients, particulate and dissolved organic matter, chlorophyll *a*, mesozooplankton, and microbial biomass to make a carbon budget for this ecosystem. We also measured primary and secondary production, community respiration rates, vertical particle flux and fecal pellet production and grazing. With observations arranged along a gradient of increasing integrated dissolved inorganic nitrogen drawdown (ΔDIN; 0.027–0.74 mol N m^{-2}), changes in DIC in the upper water column (ranging from 0.2 to 4.7 mol C m^{-2}) and gas exchange (0–1.7 mol C m^{-2}) were combined to estimate early season net community production ($_s$NCP; 0.2–5.9 mol C m^{-2}) and then compared to organic matter inventories to estimate export. From a phytoplankton bloom dominated by *Phaeocystis antarctica*, a high fraction (up to ~60%) of $_s$NCP was exported to sub-euphotic depths. Microbial respiration remineralized much of this export in the mid waters. Comparisons to short-term (2–3 days) drifting traps and a year-long moored sediment trap capturing the downward flux confirmed that a relatively high fraction (3–6%) of the export from ~100 m made

Domain Editor-in-Chief
Jody W. Deming,
University of Washington

Associate Editor
Jean-Éric Tremblay,
Université Laval

Knowledge Domains
Ecology,
Ocean Science

Article Type
Research Article

Part of an *Elementa* Special Feature
ASPIRE: The Amundsen Sea Polynya International Research Expedition

Received: October 21, 2015
Accepted: November 7, 2016
Published: December 9, 2016

it through the mid waters to depth. We discuss the climate-sensitive nature of these carbon fluxes, in light of the changing sea ice cover and melting ice sheets in the region.

Introduction

The Southern Ocean (south of 50°S) plays a disproportionate role in the global carbon cycle, accounting for approximately 25% of the oceanic uptake of atmospheric CO_2 from just 10% of the global ocean surface (Takahashi et al., 2002, 2009). This CO_2 exchange is driven by a balance of contributions from physical (e.g., cooling, deep convection) and biological (e.g., photosynthesis, remineralization) processes. The latter drive the biological pump, whereby phytoplankton photosynthesis reduces the surface pCO_2 and contributes to a net uptake of carbon. The total primary production of the Southern Ocean is ~2 Pg C yr^{-1}, with an interannual variability of ± 4% (Arrigo et al., 2008). This productivity is in part due to macronutrients that are generally abundant year-round on Antarctic continental shelves (Moore et al., 2013). The efficiency of the soft-tissue biological pump, controlling how much organic carbon sinks to depth, depends on the extent to which surface macronutrients are depleted (Sarmiento et al., 2004) among other factors (Frost, 1984; Ducklow et al., 2001; Steinberg et al., 2008; Armstrong et al., 2009; Herndl and Reinthaler, 2013). This efficiency, especially at high latitudes, exerts control on atmospheric CO_2 levels over thousands of years and may be linked to availability of micronutrients such as iron (Sarmiento and Toggweiler, 1984; Sigman et al., 2010; Sigman and Hain, 2012).

Primary production in the Southern Ocean shows marked seasonality and spatial variability. During summer, chlorophyll *a* concentrations on the Antarctic continental shelves are an order of magnitude higher than in the core of the Antarctic Circumpolar Current. Intense spring blooms are often associated with coastal polynyas, defined as recurring areas of open water surrounded by ice (Smith and Barber, 2007). The combination of an early sea ice retreat and the often-shallow stratification from surface warming and sea ice melt favors polynyas as biological oases (they account for 65% of the production on the continental shelf; Arrigo and van Dijken, 2003). Dominated by high-productivity regions, relative to the global ocean, the ocean south of the Antarctic convergence, roughly at 50°S, accounts for ~20% of global ocean carbon production (Behrenfeld and Falkowski, 1997), ~30% of the global biogenic silica flux (Tréguer and De La Rocha, 2013), and ~10% of global carbon export to depth (Schlitzer, 2002).

Annual biological production varies considerably among Antarctic polynyas, even when accounting for differences in size and latitude. Peak productivity measured by satellite varies from 0.5 to 3 g C m^{-2} d^{-1} (40–250 mmol C m^{-2} d^{-1}), and peak phytoplankton bloom timing varies from December to February depending on the polynya (Arrigo and van Dijken, 2003; Alderkamp et al., 2012, 2015), with some of the variance in mean chlorophyll explained by the proximity to melting ice shelves (Arrigo et al., 2015). Whether a polynya ecosystem is characterized by carbon retention (*sensu* Wassmann, 1998, where the fraction of primary production exported, e, is < 0.2) or dominated by export (e > 0.4) can vary seasonally or interannually and is sensitive to local forcing (e.g., sea ice cover, hydrography), productivity, food web structure, and bathymetry (Grebmeier and Barry, 2007), but the mechanisms, likely related to bloom magnitude and plankton community structure (Karl, 1993), are poorly understood (Boyd and Trull, 2007).

The Amundsen Sea Polynya (ASP) is the fourth largest Antarctic polynya (up to ~80,000 km^2; Mu et al., 2014), and the most productive on average (per unit area; via satellite algorithm; Arrigo and van Dijken, 2003; Arrigo et al., 2012, 2015). Summer primary production estimated by satellite typically exceeds ~1 g C m^{-2} d^{-1} (85 mmol C m^{-2} d^{-1}), with peak production of ~3 g C m^{-2} d^{-1} (250 mmol C m^{-2} d^{-1}) in January and an average annual production of 105 ± 22 g C m^{-2} (8.8 ± 1.8 mol C m^{-2}; Arrigo et al., 2015). This level of productivity is much higher than the average for the Southern Ocean (57 g C m^{-2} a^{-1}; Arrigo et al., 2012). Few *in situ* studies have been conducted in the ASP, however, because of its historic inaccessibility (Jacobs and Comiso, 1997; Stammerjohn et al., 2015). Although the circulation is not well known, the area is characterized by deep winter mixed layers, large water column inventories of meteoric water, and net annual sea ice formation related to a regular wintertime polynya (Randall-Goodwin et al., 2015). Deep mixing in the ASP may also be driven by eddies (St. Laurent et al., 2015), tides (Robertson, 2013), or drifting icebergs (Randall-Goodwin et al., 2015).

In austral summer 2010–11, the Amundsen Sea Polynya International Research Expedition (ASPIRE) visited the ASP onboard the RVIB *Nathaniel B. Palmer* (see Yager et al., 2012) to determine the mechanisms, climate sensitivity, and fate of the extraordinary phytoplankton bloom. The synthesis effort described here aims to calculate a carbon budget for the ecosystem by integrating the large suite of rate and inventory measurements obtained. Although the expedition could not sample over the entire open-water season, we report here an effort to quantify production and export in the water column at 13 stations sampled during the early phases of the bloom (late December and early January), by distinguishing summertime observations from those expected pre-bloom for Winter Water (WW; potential temperature, θ< –1.79°C, salinity, S > 34.1; see Yager et al., 2012; Wong et al., 1998; Randall-Goodwin et al., 2015). We find that the ASP

hosts an extraordinarily productive climate-sensitive ecosystem that surpasses its neighbors, including the well-studied Ross Sea Polynya, on most measures, exporting a high fraction to depth and contributing significantly to both the magnitude and efficiency of the biological pump in the Southern Ocean.

Methods

Field effort

ASPIRE explored the ASP region on board the RVIB *Nathaniel B. Palmer* between 13 December 2010 and 8 January 2011. Over the course of the expedition, a total of 68 stations (Yager et al., 2012) were sampled using a suite of instruments across an average open water area (≤ 10% ice cover; Mu et al., 2014) of 49,160 ± 9,952 km^2 (the greatest open water area during ASPIRE was 63,277 km^2 on January 8; Mu et al., 2014), while the ship's underway system continuously measured surface water properties: temperature, salinity, chlorophyll fluorescence, oxygen, and carbon dioxide concentrations (Yager et al., 2012; Mu et al., 2014). Here, we report data from 13 stations within and around the edges of the ASP (Table 1; Figure 1A) where a full suite of inventory and rate measurements was obtained from the upper water column.

Table 1. Station information[a] on location, ice conditions, bloom timing, and surface pCO_2

Station and CTD cast[a]	Latitude(°)	Longitude(°)	Seafloor depth (m)	Calendar day sampled (A)	Sea Ice conc. (%) on day sampled	First day 50% ice cover (B)	First day extended 0% ice cover (C)	First day ocean color detected (D)	Open water duration (days)	Ice-free days[d]	Bloom spin up (days, D–B)	Bloom duration (days, A–D)	Surface pCO_2 (µatm)	Air-sea CO_2 flux (mmol C m^{-2} d^{-1})	Surface mixed layer depth[g] (m)	Depth of T_{min_100} (m)	ΔDIN (mmol N m^{-2})[a]
5 (3)	–73.97	–118.03	1250	348	26	299	400	370	26	1	71	0	358	4	28	28	27
68 (87)	–71.86	–118.28	830	373	68	369	no[c]	no[c]	8	0	0	0	330	11	14	100	144
6 (4)	–73.18	–115.00	770	349	36	281	357	355	15	1	74	0	237	30	10	59	205
34 (31)	–72.96	–115.76	684	358	38	336	388	363	12	0	27	0	185	41	11	85	236
66 (85)	–72.74	–116.02	659	370	85	336	no[c]	374	14	0	38	0	171	44	10	60	248
18 (14)	–73.00	–113.30	435	355	5	323	377	342	24	0	19	13	173	43	15	68	310
13 (9)	–73.57	–112.67	550	352	0	265	318	331	56	34	66	21	265	23	42	75	369
25 (21)	–73.12	–112.00	406	356	0	278	338	333	38	15	55	23	197	38	16	80	470
50 (65)	–73.42	–115.25	1050	363	0	280	326	330	43	30	50	33	167	44	19	100	558
35 (46)	–73.28	–112.10	420	361	0	265	329	332	48	35	67	29	147	49	22	90	565
48 (61)	–73.70	–115.45	997	362	0	315	325	342	46	37	27	20	169	44	22	100	606
29 (26)	–73.35	–114.13	738	357	0	280	324	346	41	26	66	11	196	38	32	100	646
57 (72)	–73.71	–113.27	745	365	0	255	323	333	61	43	78	32	313[e]	14	81	100	740
AVE[a]	-[b]	-	733	359	20	299	346	346	33	17	49	14	224	32	25	80	394
S.D.	-	-	256	8	29	34	30	16	18	17	25	13	70	14	19	23	219
n	-	-	13	13	13	13	11	12	13	13	13	13	13	13	13	13	13
$R_{\Delta DIN}$[a]	–0.38	0.63*	–0.21	0.23	**–0.68**	–0.59*	**–0.85**	**–0.74**	**0.80**	**0.87**	0.31	**0.83**	**(–0.71)**[f]	0.39	0.54*	**0.73**	**1.00**

[a]Arranged in order of increasing nitrogen drawdown (ΔDIN), and including polynya-wide averages, with standard deviation (S.D.) and n value, and correlation (R) of each variable with ΔDIN (significant correlations: $p < 0.01$ in bold; $p < 0.05$ with asterisk)
[b]Indicates not applicable
[c]no = conditions not observed
[d]Includes occasional 1-day ice-free or ice-covered events not included in B
[e]Reflects deep mixing
[f]Improved correlation if Sta. 57 removed
[g]As defined by ΔT method described by Alderkamp et al. (2015)
doi: 10.12952/journal.elementa.000140.t001

Satellite observations

For navigation and planning purposes during the field expedition, sea ice concentration images from Moderate Resolution Imaging Spectroradiometer (MODIS) Terra (250 m resolution) were collected and delivered to the ship electronically from the Polar Geospatial Center (PGC; http://www.pgc.umn.edu/; formerly the Antarctic Geospatial Information Center), Department of Geology and Geophysics, University of Minnesota. Daily ASMR-E satellite images (12.5 km resolution) were also obtained for the 2010–11 season to provide an assessment of ice conditions over the larger ASP region and in the months prior to and after the ASPIRE sampling period. A summary of the growth of the 2010–11 summer polynya and regional changes in sea ice cover during ASPIRE can be found in Mu et al. (2014). This early opening of the polynya in the southeast was expected from historical sea ice imagery and was the reason we located a moored sediment trap (MT) in this area (Figure 1). The daily ASMR-E images were used to calculate several different measures of ice cover timing for each station. Application of these surface-associated conditions to the water column below

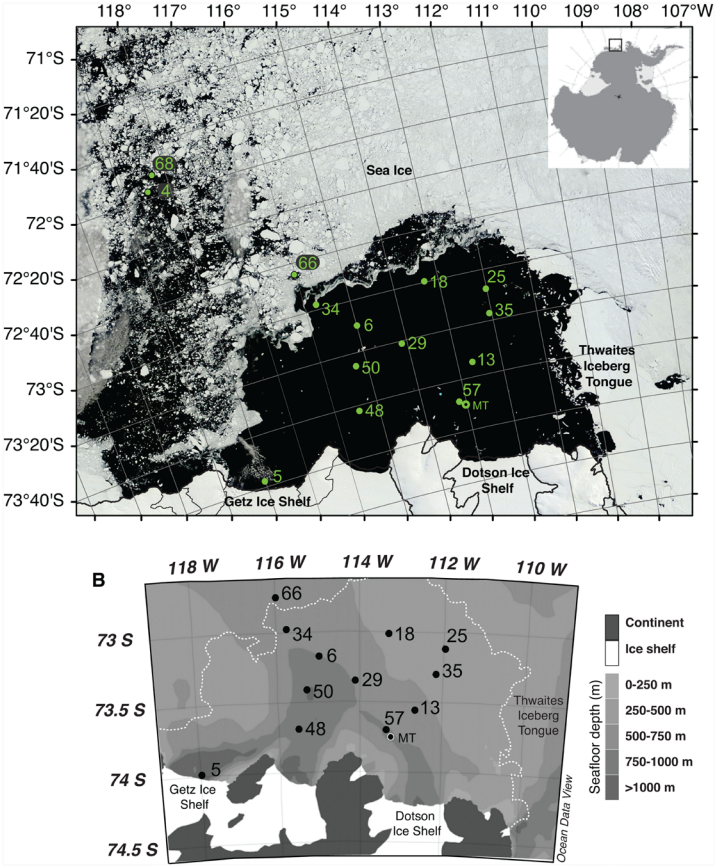

Figure 1

Study area for ASPIRE.

Maps of the study area showing the ice shelf and coastal features with numbered stations located on A) Moderate Resolution Imaging Spectroradiometer (MODIS) Terra (250 m resolution) image from 2 January 2011 showing sea ice and land ice (white) and open water (black) in the Amundsen Sea region; and on B) bathymetric contours (gray) from Nitsche et al. (2007), with the sea ice margin on 2 January 2011 shown as a white dotted line. The position of the moored sediment trap (Ducklow et al., 2015) is denoted by MT.

doi: 10.12952/journal.elementa.000140.f001

assumes that horizontal advection was minor compared to vertical controls at the satellite scale (12.5 km for ice; 1.24 km for ocean color). Some support for this assumption was found with the good correlations between surface conditions and integrated changes to the water column (see below).

Using satellite-derived sea ice concentrations for a patch of ocean surrounding each station, we noted the percent sea ice cover (sea ice concentration, %) on the day we sampled. We also calculated the *open water duration* (*OWD*, or number of open water days) as the total number of days each station location had ≤ 50% ice concentration from the date of first opening until (and including) the date of sampling, as consistent with Mu et al. (2014) and Lowry et al. (2015). In our experience, waters with ≤ 50% sea ice cover can sustain pelagic bloom initiation and development because adequate sunlight reaches the water column. For each station patch, the first day of the year that ice concentration dropped ≤50% was noted. At some stations, sea ice concentration went up and down for several weeks, so we summed the total number of days ≤ 50% ice cover between the first observation until (and including) the day of sampling. Any days in between with a sea ice concentration > 50% were not counted as part of *OWD*. The uncertainty in OWD was calculated as the standard deviation of the number of open water days when calculated with a range of sea ice concentration thresholds (10–90%). We also noted the first date after which the region stayed ice-free (0% ice cover) continuously for more than a few days and calculated similarly the number of ice-free days.

We obtained for each station a time series of ocean color by MODIS Aqua (1.24 km resolution) to identify the first day that ocean color was observed. At some stations (e.g., 5 and 6), ocean color was detected early, but the time series was flat at very low levels (< 0.05 μg L^{-1}), in which case we defined the first day as the day ocean color began to increase above baseline. "Bloom spin up" was estimated by the number of days between the first day of ≤ 50% ice cover and the first day of ocean color. Bloom duration was estimated by the number of days between the first day of ocean color increase and the day of sampling. Bloom duration could equal zero if the day of sampling occurred before the start of noticeable ocean color (as it was at 5 of the 13 stations). Although most stations showed increases in color over the bloom duration time period, it was not always a monotonic increase; sometimes ocean color decreased during the bloom duration interval. In summary, four ice-cover-associated, bloom-related time scales were determined: 1) open water duration (OWD; days < 50% ice concentration before a station was sampled); 2) ice-free days (days of 0% ice cover before station was sampled); 3) bloom spin up time (number of days between the first observation of open water (≤ 50%) and an initial increase in ocean color); and 4) bloom duration (number of days between the initial increase in ocean color and the day of sampling).

Water sampling

Hydrographic profiles and discrete water samples were collected from each station using a conventional shipboard conductivity-temperature-depth (CTD; Sea-Bird 911+) sensor and a 24 × 10 L Niskin bottle rosette sampler (General Oceanics). Potential temperature (θ) and salinity (S) were recorded continuously as a function of depth and at the moment of Niskin bottle closure. Continuous dissolved oxygen (DO) profiles were measured using a Sea-Bird SBE-43 dissolved oxygen sensor on the CTD and calibrated as reported in Mu et al. (2014). A few samples reported here were collected similarly using a trace-metal-clean CTD-rosette system (see Sherrell et al., 2015) that was deployed at the same location just before or after the conventional CTD. Some hydrographic data from Sta. 4 (near Sta. 68; Figure 1A) were included as they proved useful for comparison, even though this station was not covered by the full suite of measurements.

Water samples were collected and processed according to standard protocols (Knap et al., 1996; Dickson et al., 2007) for dissolved inorganic carbon (DIC), alkalinity (ALK), nutrients, chlorophyll *a* (Chl *a*), particulate and dissolved organic carbon (POC, DOC), particulate and total dissolved nitrogen (PN, TDN), and particulate phosphorus (PP; Planquette and Sherrell, 2012; Planquette et al. 2013). Samples for the oxygen isotope ratio ($\delta^{18}O$) of water (H_2O) were collected and analyzed as described by Randall-Goodwin et al. (2015). Samples from the same depths and stations were also collected for microbial biomass and activity (see below; Williams et al., 2016). With a few exceptions (to characterize water mass end members), this paper focuses on samples collected from the upper 100 m of the water column. Seafloor depths in the area ranged from 300 to 1300 m (Figure 1B; Nitsche et al., 2007), although the 13 stations discussed here were all deeper than 400 m (Table 1). Surface mixed layer depths were calculated following Alderkamp et al. (2015), as the shallowest depth at which the potential density (σ_θ) was 0.02 kg m^{-3} greater than at the surface (Cisewski et al., 2008; Alderkamp et al., 2012).

Inorganic nutrients, inorganic carbon, and organic matter analysis

Dissolved inorganic nutrient samples were pre-filtered through 0.45-µm polycarbonate syringe filters, kept refrigerated, and analyzed onboard the ship within 1 day of sampling. Nitrate (NO_3^-), nitrite (NO_2^-), ammonium (NH_4^+), phosphate (HPO_4^{2-}), and silicic acid ($Si(OH)_4$) were measured using a five-channel Lachat Instruments QuikChem FIA+ 8000s series autoanalyzer in conjunction with a Lachat Instruments XYZ AutoSampler (ASX-500 Series), two Lachat Instruments RP-100 Series peristaltic Reagent Pumps, and Omnion Software, version 3.0.220.02. The nitrate + nitrite analysis uses the basic method of Armstrong et al. (1967), with minor improvements for precision and ease of operation. Nitrate was first reduced to nitrite using a cadmium reduction column and imidazole buffer as described by Patton (1983). Sulfanilamide and N-(1-Napthyl) ethylenediamine dihydrochloride react with nitrite to form a colored diazo compound. Nitrite analysis was performed on a separate channel, omitting the cadmium reductant. Ammonium was determined using the indophenol blue method modified from ALPKEM RFA methodology (EPA, 1984). Total dissolved inorganic nitrogen (DIN) was calculated by summing $NO_3^- + NO_2^- + NH_4^+$. The phosphate method was a modification of the molybdenum blue procedure of Bernhardt and Wilhelms (1967), in which phosphate was determined as reduced phosphomolybdic acid employing hydrazine as the reductant. The silicic acid method was based on Armstrong et al. (1967), as adapted by Atlas et al. (1971). Addition of an acidic molybdate reagent forms silicomolybdic acid, which was then reduced by stannous chloride. Detection limits ($NO_3^- + NO_2^-$ = 0.075 µmol L^{-1}; NO_2^- = 0.009 µmol L^{-1}; NH_4^+ = 0.040 µmol L^{-1}; HPO_4^{2-}= 0.022 µmol L^{-1}; and $Si(OH)_4$= 1.90 µmol L^{-1}) and precision ($NO_3^- + NO_2^-$ = ± 0.0076 µmol L^{-1}; NO_2^- = ± 0.0009 µmol L^{-1}; NH_4^+ = ± 0.0041 µmol L^{-1}; HPO_4^{2-} = ± 0.0023 µmol L^{-1}; and $Si(OH)_4$= ± 0.193 µmol L^{-1}) were determined using multiple runs of standards prepared in low nutrient seawater. Samples with negative values following calibration using standard curves were converted to zeros.

Samples for DIC were preserved with mercuric chloride and sealed (Dickson et al., 2007), and then stored cool and dark until analysis using the SOMMA at UGA (Johnson et al., 1993; Cooley and Yager, 2006). Accuracy was confirmed with Certified Reference Material from University of California, San Diego (CRM; Dickson et al., 2003) and precision was determined to be better than ± 1 µmol kg^{-1} using duplicate samples from surface and 200 m depths. Alkalinity measurements were made on the same samples (following DIC analysis) using a programmable open-cell potentiometric titration system (Dickson et al., 2003; Cooley and Yager, 2006). Accuracy was established by acid-calibration using multiple daily runs of CRM. Precision was determined to be ± 5 µmol kg^{-1} using replicate samples run on multiple days.

Samples for particulate organic carbon (POC) and nitrogen (PN) were collected by cleanly filtering 100–600 mL of seawater onto a 25-mm diameter, combusted GF/F filter (nominal pore size of 0.7 µm) which was then folded sample side in and frozen at –80°C. Samples were processed at Rutgers University and analyzed using a Carlo-Erba CHN analyzer (Hedges and Stern, 1984). Precision, based on replicate filtered volumes from the same Niskin bottle, was ± 5% for most samples, but was occasionally higher. Samples for particulate phosphate (PP) were collected separately from the same depths and locations as part of a trace metal suite and analyzed separately using a Thermo-Finnigan Element I HR-ICP-MS (Sherrell et al., 2015; Planquette and Sherrell, 2012; Planquette et al., 2013). Precision was ± 5%.

Samples for DOC and TDN were collected cleanly from the filtrate of the POC/PN samples and stored frozen until processed at the Georgia Institute of Technology by Shimadzu TOC-5000 analyzer with an associated TNM-1 Total Nitrogen Measuring Unit. Precision was ± 4%. Residual dissolved organic nitrogen (DON) was calculated by subtracting DIN from TDN. This approach involves taking the difference between two relatively large numbers, thus precision of relatively small DON concentrations is strongly affected by the precision of the DIN and TDN analyses.

Organismal abundance and biomass analysis

Water column Chl *a* concentration (used as a proxy for algal biomass) was measured onboard ship using acetone extraction and a spectrofluorometer (Alderkamp et al., 2015). Shipboard values were calibrated against a second set of samples collected similarly, flash-frozen in liquid N_2, stored at –80˚C, and analyzed at Mote Marine Lab using HPLC (Wright et al., 1991; see Alderkamp et al., 2015). CHEMTAX (Mackey et al., 1996; Wright et al., 1996; 2010) was applied to determine the relative abundance of phytoplankton classes based on pigment analysis (see Alderkamp et al., 2015).

Bacterial abundance samples were collected in triplicate, preserved using 1% paraformaldehyde, and deep frozen (–80 ˚C) until they were counted at The University of Georgia with flow cytometry and SYBR Green I nucleic acid staining (Marie et al., 1997). Abundance was calibrated with polystyrene beads, and values were crosschecked using DAPI and epifluorescence microscopy (Porter and Feig, 1980). Abundance was converted to bacterial carbon (BAC) using a conversion factor (25 fg C $cell^{-1}$; Simon and Azam, 1989). Precision was ± 3%.

Microzooplankton abundance and biovolume were determined at select depths and stations using microscopy (Goswami, 2004). Samples were gently siphoned through silicon tubes into 300 ml amber colored glass bottles, fixed in acidic Lugol's solution (2% final concentration), and kept cool and dark until analysis. Biovolume calculations followed the HELCOM (2014) manual on appropriate geometrical shapes when making length-width measurements for each individual species. Biovolumes were corrected for shrinkage due to preservation (vol × 1.33; Stoecker et al., 1994). Heterotrophic/mixotrophic microplankton cell volumes were converted to cell carbon (Menden-Deuer and Lessard, 2000) for loricate and aloricate ciliates (CIL), and dinoflagellates (DINO).

Heterotrophic nanoflagellates (HNAN) were counted by flow cytometry (Christaki et al., 2011). Each sample was stained with SYBR Green, at final concentration of 1:10000 and a minimum staining time of 10 minutes in the dark. The flow rate was ~250 μL min^{-1}. Both green and red fluorescence were use to discriminate between autotrophs and heterotrophs. Data acquisition was 5–10 minutes depending on concentration of the sample (or depth). Samples with > 1200 event $second^{-1}$ were diluted to allow a correct measurement. The detected abundance was checked against counts of DAPI filters. HNAN biomass was converted from abundance data assuming 3.5 μm^3 per cell biovolume (Vaqué et al., 2002) and 220 fg C μm^{-3} (Børsheim and Bratbak, 1987).

Mesozooplankton biovolume and abundance were determined as described by Wilson et al. (2015) and converted to biomass (ZOOP) for both daytime and nighttime tows using conversion factors from the literature (Gallienne et al., 2001; Forest et al., 2012; Trudnowska et al., 2014).

Biological rate measurements

Phytoplankton net primary production (NPP) rates were determined for 6 light depths in the upper 100 m using standard ^{14}C-bicarbonate incubations (Steeman-Nielsen, 1952; Knap et al., 1996) in on-deck incubators with light-filtering screens to match *in situ* light levels. Bacterial production (*BP*) rates were determined using ^3H-leucine incorporation as described by Williams et al. (2016). Microbial community respiration (*MCR*) rates were determined for near-surface and subsurface depths by changes in CO_2 concentrations over 48 hours in dark incubations, as described in Williams et al. (2016).

An upper bound for microzooplankton grazing rate was estimated as part of another experiment (R. Swalethorp, personal communication) by measuring potential microzooplankton growth rates at a peak bloom station using large volume incubations over a two-week period. Seawater was collected from the fluorescence maximum at Sta. 35 (12 m depth; *in situ* conditions were determined later to be: Chl *a* = 8.6 μg L^{-1}, DIN = 10.4 μmol L^{-1}, DIP = 0.76 μmol L^{-1}). Two treatments were carried out in triplicate 12-L containers: whole water and 200-μm filtered (to remove mesozooplankton). Because we did not know their *in situ* concentrations until afterwards, nutrients (15 μmol L^{-1} NH_4Cl and 1 μmol L^{-1} Na_2HPO_4) were added at the start and containers were incubated at *in situ* light and temperature (0 ± 0.5 ˚C) for 15 days. Samples for ciliate and dinoflagellate biomass were taken at Day 2, 4, 7, 10, 13 and 15 and analyzed following the same procedure as described above for the *in situ* biomass samples. The rate of increase in biomass over time in each of the size fractions was estimated and compared initially using linear regression. Growth rates for the microzooplankton were then calculated for each time step using the following equation:

$$\mu = \frac{ln(B_{t0+1}) - ln(B_{t0})}{B_{t0+1} - B_{t0}} \quad (1)$$

where B is the microzooplankton biomass at sampling day t_0 and at the following sampling day t_{0+1}. Grazing rate was determined from growth rate (Bjørnsen and Kuparinen, 1991) and assumed to be equal to carbon demand (= growth + respiration, assuming a gross growth efficiency of 0.3; Straile, 1997, Landry and Calbet 2004, Chen and Liu, 2011). This assumption would overestimate the grazing rate if many of the microzooplankton were mixotrophs or feeding on other protists and heterotrophic nanoflagellates.

Mesozooplankton grazing rates were measured for both night and day samples from 7–8 depth intervals (3–4 intervals in the upper 100 m) at 6 stations (13, 25, 35, 50, 57, 68) using the gut fluorescence method (Slaughter et al., 2006; Bernard et al., 2012). Gut pigments were calculated following Strickland and Parsons (1972) and converted to grazing rates using a temperature dependent gut evacuation rate (Dam and Peterson, 1988). Grazing rates were converted to carbon assuming a C:Chl *a* ratio of 50 (Atkinson et al., 1996) and integrated over the upper 100 m, 100–350 m, or lower water column (> 350 m).

Sediment trap material sampling and analysis

Sinking particulate material was collected using two kinds of sediment traps deployed during ASPIRE: 1) a year-long moored trap, which was deployed on 16 December 2010 at a single location in the deep central trough (MT; Figure 1) with collection at 375 m below the sea surface (Ducklow et al., 2015); and 2) a three-tiered, drifting sediment trap array (e.g., Knauer et al., 1979; Karl et al., 1996; Munson et al., 2015), which was deployed at two stations (35 and 57; Figure 1) for 2–3 days to capture sinking particles at 60, 150, and 300 m depths. Details of the moored trap methods are reported elsewhere (Ducklow et al., 2015). For the drifting traps, an array of polycarbonate collection tubes attached to a fiberglass and stainless steel frame was secured to a polyester rope at each of three depths and the entire array was suspended from a series of floats and buoys. Each trace-metal-clean collection tube was 7.6 cm inside diameter and 60 cm long, with a polycarbonate machined cone in the bottom end, threaded to attach to the neck of a narrow mouth high-density polyethylene 250 mL bottle (Munson et al., 2015). Trap tubes were filled prior to deployment with 0.2 µm filtered (Pall Acropak-200 capsule filter) clean brine made by partial freezing of deep water collected using trace metal clean techniques (Sherrell et al., 2015) to minimize loss of particulate material by mixing and exchange with ambient seawater.

Additional collection tubes were assembled similarly for microbial measurements, except the collection bottles were sterile 50 mL centrifuge tubes (Falcon) and the brine was made from filter-sterilized seawater. All tubes were tightly covered until just before deployment. After recovery, brine in the trap tubes was siphoned off to the level of the top of the collection bottle using clean plastic tubing. The sedimented material trapped in the brine-filled 250 mL bottle was vacuum filtered through one or a series of 0.45µm Supor® (Pall) polysulfone filters (3–4 filters used sequentially for 60-m material, as the mass of particles caused filter clogging), which were transferred to acid-cleaned polystyrene Petri-slides and frozen at sea. Total processing time following trap array recovery was ~6 hours, and trap tubes were kept at 0–5°C in the dark while awaiting processing. Upon return to Rutgers University, filtered samples were subjected to total acid digestion in a hot mixture of nitric and hydrofluoric acid and analyzed for P and other elements by HR-ICP-MS, following the methods of Planquette and Sherrell (2012). Total dry weight was determined at The University of Georgia on triplicate samples collected onto pre-weighed glass-fiber filters (GF/F; nominal pore size 0.7 µm; no salt corrections were made).

Elemental fluxes were calculated for each trap tube using cross-sectional area of tube and duration of deployment. The C flux was calculated from P flux and each station's ΔPOC:ΔPP ratio. Fluxes for the individual tubes at each depth replicated well, yielding mean P fluxes with 8–10% relative standard deviation (RSD; n = 3–4 tubes per depth) for all trap arrays except the 150-m array (28–29% RSD, n = 3–4). Replication for the dry weights also varied with depth and deployment (7–47%, n = 3). The trapping efficiency of the drifting traps is unknown under ASPIRE field conditions. Comparisons to the moored trap and to water column calculations should be qualitative only.

Water column calculations

To distinguish biological impacts from physical effects on the carbon and nutrient budgets of the upper water column, we calculated for all measured inventories and sample depths the difference between the observed concentrations and those expected from physical processes (mixing and ice melt) alone. These calculations required assumptions to be made about the relevant integration depth and the initial condition of the wintertime water column, which we discuss below.

The choice of integration depth for the upper water column, typically the surface mixed layer or euphotic zone, had to consider the rapid temporal changes occurring during the ASPIRE expedition (e.g., a shallowing pycnocline, along with dense blooms reducing light penetration). The surface mixed layer depths observed at the time of sampling were shallow, but variable (average = 25 ± 19 m; ranging from 10 to 81 m; Table 1). The

euphotic zone at the time of sampling was also relatively shallow, but typically deeper than the mixed layer and similarly variable (average = 35 ± 19, ranging from 21 to 94 m). Our choice of integration depth had to balance the need to catch early season production mixed to depth, without missing production lost to deep remineralization later in the season. The process was complicated further by not knowing enough about the physical dynamics of the region. On balance, after trying several different approaches, we chose to integrate upper water column inventories and their differences over a relatively deep interval (up to 100 m) to allow for the high probability of mixing during the early season when the seasonal pycnocline was likely deeper or weaker. Going that deep meant that we had to be mindful of deep-water intrusions from below. Because of spatial heterogeneity of water masses (see Figure 2 and Results below), we took a station-by-station (local) approach, rather than use the same depth for every station.

The upper 100 m of the water column of the ASP was primarily Antarctic Surface Water (AASW) overlying remnant Winter Water (WW), the former freshened by sea ice melt and warmed by solar radiation (Yager et al., 2012). Often in polar oceans, dilution by meltwater is corrected by scaling (normalizing) observations to a single salinity (see, for example, Sweeney et al., 2000). In the ASP, however, the upper 100 m exhibited additional and variable contributions from shoaling, modified Circumpolar Deep Water (mCDW) made buoyant by glacial ice melt (Randall-Goodwin et al., 2015). Thus, two sources of meltwater (sea ice and glacial ice) modified the upper 100 m but to varying degrees, depending on the influence from mCDW at depth (Figure 2). For example, the θ-S curve for Sta. 68 in the west near the shelf break (Figure 1A) shows seawater at 100 m with properties near canonical WW, which freshens and warms to the surface (Figure 2), indicating very little influence from mCDW. In contrast, Sta. 66 to the south and east (Figure 1A), for example, exhibits similar warming and freshening from 60 m to the surface, but below that, the waters exhibit warming from mCDW (Figure 2).

Inventory data from all samples of unmodified WW (as defined by θ< –1.75°C and S > 34.1) collected during ASPIRE were averaged to estimate biogeochemical "end member" properties (± 1 STD; n = 19). We did the same analysis for the samples of mCDW (as defined by S > 34.5; depth > 400 m) to estimate similarly its average biogeochemical "end member" properties (± 1 STD; n = 41).

For a subset of seawater samples, we used tracers to determine meltwater fractions (Randall-Goodwin et al., 2015; see below) and then applied an end-member mixing model to account for the expected contributions from both sea ice and glacial meltwater. Critical to this effort was defining the winter seawater conditions. We intended to use either WW or a winter baseline estimated by the concentrations observed at 100 m, which in the ASP were always below the euphotic zone and the base of the summer mixed layer (Tynan, 1998; Prézelin et al., 2000; Yager et al., 2012; Schofield et al., 2015). However, because of variable subsurface inputs from mCDW (see Figure 2), even temperature and salinity observations at 100 m were highly variable from station to station, and consequently so were other inventory contributions from mCDW. Thus, to approximate wintertime conditions for each station (as the WW end member), we used the deepest value within the upper 100 m that approximated WW without input from mCDW. We determined this value to be at the depth of the minimum temperature within the upper 100 m (T_{min_100}; noting that for many stations, the absolute T_{min} for the full-depth profile was well below 100 m). In 5 of the 13 stations (29, 48,

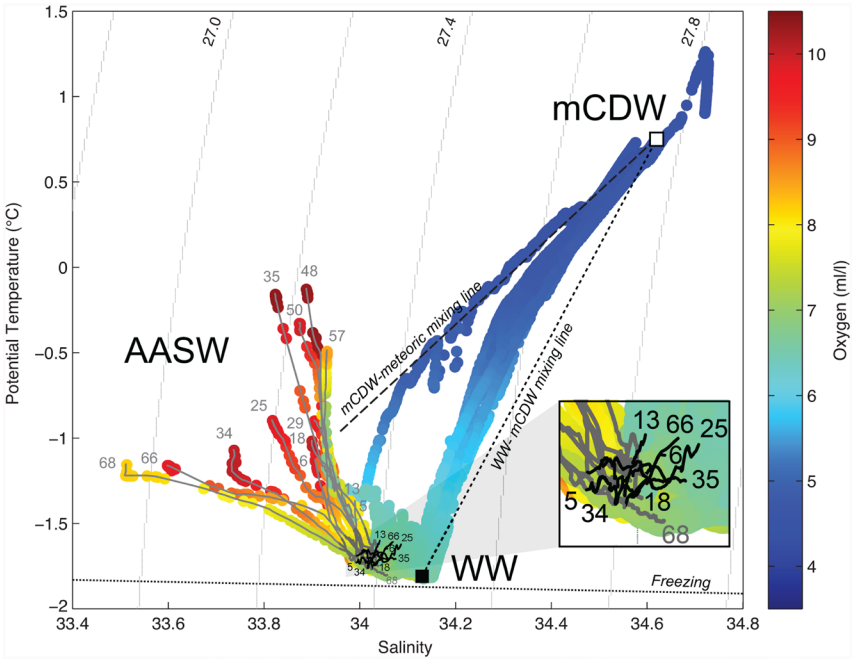

Figure 2

Water masses in the ASP.

Temperature-salinity diagram, with Winter Water (WW), modified Circumpolar Deep Water (mCDW), and Antarctic Surface Water masses, showing the full 13 station profiles (labeled with station numbers in gray at the surface) using oxygen concentration (colored according to the legend). Solid gray lines indicate the parts of the profiles used for the upper water column integrations. Black segments (also numbered at bottom) indicate the lower parts of the upper 100 m profiles of the eight stations (see Table 1) that were not used in the integration because of the intrusion of mCDW at depth, indicated by curving up and right (see inset) towards the mCDW water mass endpoint. The dotted gray line is the seawater freezing line. The black, short-dashed line is the mixing line between WW and mCDW. The black, long-dashed line shows the mixing line between mCDW and glacial melt (meteoric) water.

doi: 10.12952/journal.elementa.000140.f002

50, 57, 68), T_{min_100} was observed at 100 m, so the outcome was identical to the original plan. At the other 8 stations, however, T_{min_100} ranged from 28 to 90 m (Table 1).

Freshwater fractions for sea ice meltwater (FWF_{sim}) and from meteoric sources derived from glacial melt and snow (FWF_{met}) were determined with the tracer $\delta^{18}O$ in the same fashion as described by Randall-Goodwin et al. (2015), except that instead of using a regional CDW $\delta^{18}O$ end member, we used the value of $\delta^{18}O$ at T_{min_100} (as described above) as the local WW end member for each station. This approach assumes that the wintertime upper water column is well mixed and allowed an estimate of the local meltwater contributions relative to WW, i.e., relative to winter concentrations prior to the most recent spring melt. It is in contrast to the approach taken by Randall-Goodwin et al. (2015), who integrated over longer and wider time and space scales using regional CDW as the $\delta^{18}O$ end member, i.e., including regional modification of CDW by net annual sea ice production and melt and net annual contribution from meteoric sources. Because the inherent time period covered by our estimates of freshwater contributions included only the spring melt, they do not include the negative contribution from sea ice formation (due to brine rejection), and only include a relatively short interval for meteoric contributions. Calculated in this way, freshwater contributions to the upper 100 m and relative to WW ranged from 0 to 2% for sea ice melt and from 0 to 0.5% for the meteoric water.

Sea ice and glacial melt contribute freshwater that reduces seawater salinity, but it may also contribute some inorganic carbon, nutrients, and organic matter to the ocean. Because ASPIRE did not have an ice-sampling program onboard in 2010–11, sea ice melt and glacial meltwater contributions for nutrients and organic matter were estimated from literature values of these endmembers (X_{sim} and X_{met}, respectively, for any parameter "X"), some of which came from the ASP region just two years prior to ASPIRE. For sea ice melt (Fransson et al., 2011; Thomas and Dieckmann, 2010), we assumed DIC_{sim} = 270 μmol L^{-1}, DIN_{sim} = 2 μmol L^{-1}, DIP_{sim} = 0.3 μmol L^{-1}, DOC_{sim} = 1000 μmol L^{-1}, DON_{sim} = 70 μmol L^{-1}. For glacial melt (Rysgaard et al., 2011), we assumed DIC_{met} = 170 μmol L^{-1}, DIN_{met} = DIP_{met} = 0 μmol L^{-1}, DOC_{met} = 50 μmol L^{-1}, DON_{met} = 0 μmol L^{-1}.

Thus, the expected concentration (X_{exp}) was determined using the freshwater fractions and their end members:

$$X_{exp} = X_{sim}*FWF_{sim} + X_{met}*FWF_{met} + X_{sw}*SWF \quad (2)$$

where X_{sw} is the seawater concentration at depth of T_{min_100}, and

$$1 = SWF + FWF_{sim} + FWF_{met} \quad (3)$$

The observation (X_{obs}) at each sample depth was then measured against X_{exp}, derived from physical contributions, to calculate the biologically-driven change.

The biological change in the total inorganic nitrogen inventory for the upper water column (ΔDIN, mmol N m^{-2}) was calculated by trapezoidal integration of the difference between observed and expected DIN concentrations down to the depth of T_{min_100}. The integrated changes in other chemical inventories (ΔDIC, ΔDIP, ΔPOC, ΔPN, ΔPP, ΔDOC, ΔDON) were calculated similarly. Because particles can move independently of water masses, we assumed winter and meltwater end members for particulate matter to be zero. This assumption may overestimate particulate production.

Seasonal changes in the surface water column inventories of biomass (ΔChl *a*, ΔBAC, ΔHNAN, ΔDINO, ΔCIL, and ΔZOOP) were calculated similarly to particulate matter (zero meltwater and winter end members), except that we integrated to 100 m at all stations. The possibility of deep water contaminating the signal was small because biomass decreases dramatically with depth. For overwintering organisms, this use of deeper integrations and zero wintertime end members would overestimate their springtime growth. Thus, our integrated biomass increases are considered upper limits, but the export calculations below are conservative.

Air-sea CO_2 gas exchange during the ice-free period was included in the carbon budget calculation. Although photosynthesis may take some time to set up a large pCO_2 gradient, melting sea ice contributes freshwater and alkalinity to the surface layer, reducing surface pCO_2, and setting up the potential for gas exchange even before the bloom occurs (Mu et al., 2014). Sea ice algal productivity may also reduce the near surface pCO_2 (Yager et al., 1995; Miller et al., 2002). The rate of gas exchange, or the CO_2 *flux density* (CO_{2flux}; mmol C m^{-2} d^{-1}), was estimated from underway pCO_2 measurements as described by Mu et al. (2014). Carbon gained or lost to the surface waters by gas exchange (*GasEx*) was estimated for each station by using the ΔpCO_2 observations at each station, calculating CO_{2flux} for that station using the average wind speed for the region during the time of ASPIRE (measured shipboard; u_{10} = 8.7 ± 3.5 m $second^{-1}$; n = 6209; see Mu et al., 2014), and applying that rate over the number of ice-free days to get the total carbon exchanged. This approach might overestimate gas exchange because it assumes a steady gradient and the biological component of the pCO_2 gradient likely took some time to build up to observed levels. This calculation does not include any gas exchange that may occur through full or partial sea ice cover, however. The net CO_2 uptake at all stations, regardless of bloom status, reflects the modest pCO_2 reduction (56 μatm) from sea ice alkalinity in addition to biological drawdown (see Mu et al. 2014 for complete discussion of mechanisms).

Because all 13 stations were undersaturated with respect to atmospheric pCO_2 (Mu et al., 2014), they likely all received some DIC replenishment from air-sea exchange. Thus, the observed ΔDIC would underestimate biological drawdown if we did not account for this gas exchange. The seasonal net community production, *s*NCP (mol C m^{-2}), then, was estimated by adding *GasEx* to the observed missing inorganic carbon inventory, ΔDIC:

$$sNCP = \Delta DIC + GasEx \quad (4)$$

For stations where the DIC data were not available, ΔDIN was converted to ΔDIC using the Redfield ratio (which was also equal to the average ΔDIC:ΔDIN for the region of 6.6 ± 0.9, $n = 7$). To calculate NCP as a rate (mmol C m^{-2} d^{-1}) rather than a seasonal quantity, we divided *s*NCP by the open water duration (OWD) for each station (see also Ducklow et al., 2015).

A carbon budget was constructed for the upper water column of the ASP (Figure 3; see also Table 8 and Figure 11 as described in Results) to determine consistency within individual inventory and rate measurements, calculate inferred export, and compare these to direct measures of export (e.g., sediment traps). We assumed that the accumulated changes in total carbon in the upper water column could be accounted for among the quantities we measured, and that the sum of the changes in total carbon (ΔTotalC) would add up to zero:

$$\Delta TotalC = sNCP - \Delta POC - \Delta DOC - \Delta ZOOP - ExportC = 0 \quad (5)$$

Seasonal Export C (sExportC, mol C m^{-2}) was thus calculated as:

$$sExport\ C = sNCP - \Delta POC - \Delta DOC - \Delta ZOOP \quad (6)$$

As we have no observations for wintertime biomass in the ASP, the most conservative estimate for export would be to include all observed biomass as new biomass produced locally since winter. Thus, export is determined by subtracting these values from *s*NCP. The export calculation would increase if some of the observed biomass was already present before the springtime ΔDIC drawdown.

Because we had some (although not many) migrating zooplankton, we used the larger of the two inventories ($\Delta ZOOP_{day}$ or $\Delta ZOOP_{night}$) to estimate the maximum ΔZOOP. We did not account for carbon transported to depth and respired or released by migrating zooplankton (e.g., Steinberg et al., 2000) because subsurface mesozooplankton biomass and respiration rates were low (0.01-0.11 mmol C m^{-2} and < 0.01 mmol C m^{-2} d^{-1}, respectively; Ducklow et al., 2015).

As with *s*NCP, the seasonal quantity, *s*ExportC, was converted to a rate (ExportC, mmol C m^{-2} d^{-1}) by dividing by OWD. The exported fraction, based on seasonal quantities only, was estimated by dividing *s*ExportC by *s*NCP. Two different estimates of export efficiency, based on relative rates, were calculated by dividing NCP or ExportC by ASPIRE's best estimate of primary production, NPP. A turnover time (*s*NCP/NPP, in days) was also estimated by dividing the seasonal production by the daily production rate.

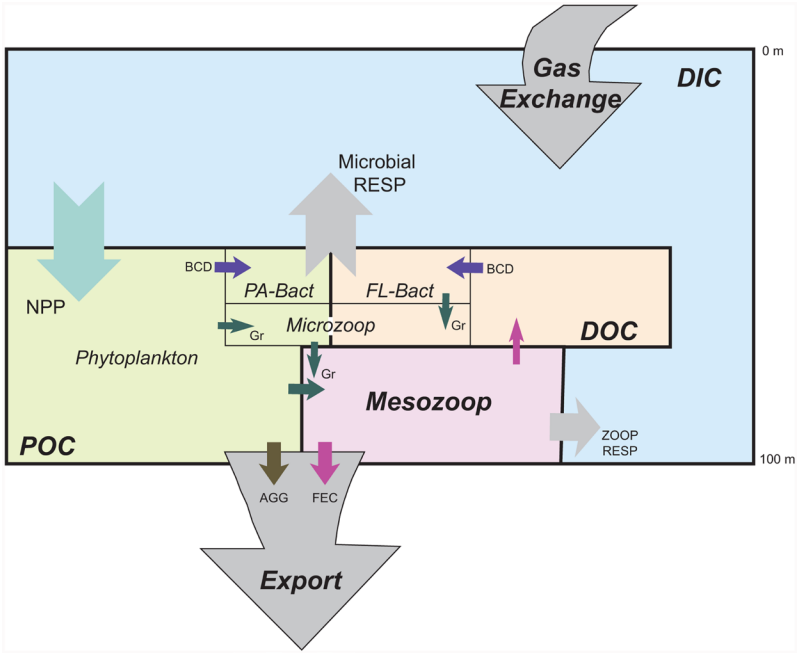

Figure 3

Carbon inventories and fluxes in the upper water column of the ASP.

A cartoon depiction of the one-dimensional carbon budget for the upper water column of the ASP. Major carbon inventories include dissolved inorganic carbon (DIC), particulate organic carbon (POC), dissolved organic carbon (DOC), and mesozooplankton (Mesozoop). Microbial biomass, including phytoplankton, microzooplankton (Microzoop), particle-associated (PA) and free-living (FL) bacteria (Bact) are distributed into the major carbon inventories. Exchanges between the inventories include net primary production (NPP), microbial respiration, zooplankton respiration (Zoop Resp), grazing (Gr), bacterial carbon demand (BCD), aggregation (AGG), and fecal pellet production (FEC). Additions to or losses from the upper water column occur through gas exchange and export.

doi: 10.12952/journal.elementa.000140.f003

Uncertainties

Uncertainties in the export calculations were not formally propagated through each equation because known uncertainties associated with analytical measurements were small compared to the potential errors associated with endmember choices, interpolation between sampled depths, and assumptions about a one-dimensional water column. After working with these data, it became clear that the calculations were most sensitive to variables that were not very well quantified. In the interest of trying to gain the best insight about this system, we present these analyses with the caveat that the final export values are estimates and probably have an uncertainty of ± 50%. We base this error estimate on rough error propagation efforts combined with a sense of how the final values could vary when calculated in different ways. The largest potential source of error came from uncertainty associated with the choice of WW endmembers, because small differences were then integrated up through the water column. For example, at Sta. 66 (discussed above), integrating to the higher NO_3^- concentration observed at 100 m (instead of using the value at T_{min_100} at 60 m) would give a value for ΔDIN that was 49% larger than the value we determined. Choosing regional averages or using WW endmembers increased ΔDIN even further because of the higher NO_3^- concentrations. The decision to use T_{min_100} to define the endmembers was therefore conservative in terms of estimating the biological impacts on carbon and nutrients.

Cross checks

Because bacterial and microzooplankton biomass are included operationally in the DOC and POC inventories, we did not include them separately in the export calculation. We looked internally, however, at the individual carbon components to see if the seasonal increases were consistent with changes in biomass and biological rate measurements for each of those pools. For example, although oversimplified, we estimated algal carbon (diatoms + *Phaeocystis*) as follows:

$$Algal\ C = \Delta POC - \Delta CIL - \Delta DINO - \Delta HNAN - \Delta BAC \quad (7)$$

Algal C was then compared to Chl *a* estimates to see if the C:Chl *a* ratios were consistent with the dominant phytoplankton at each station. Because a significant fraction of bacteria were either particle-associated (PA-BACT, Figure 3; Williams et al., 2016) or potentially collected on the GF/F filter used for the POC filtration, they were included as part of the POC.

Statistical reporting

Except where noted, average values are reported with ± 1 standard deviation (S.D.) and the number of values (n) used to calculate the mean. Significant differences between averages were determined by T-test using $t_{0.05[n1+n2-2]}$ as the critical value (Sokal and Rohlf, 1981). When calculations were made using averages, errors were propagated according to Bevington (1969). Pearson product-moment correlation coefficients (R) were used to relate two sets of values; a significant correlation was determined if R was greater than the critical value reported ($p < 0.01$ or $p < 0.05$) for a given number (n) of data pairs (Sokal and Rohlf, 1981). Model I Linear regression (Sokal and Rohlf, 1981) was applied to calculate rates of change in incubations, where the x-axis was time (measured without error); rates were based on slope calculations and are reported with ± 95% confidence interval. Slopes were considered not significantly different when their 95% confidence intervals overlapped.

Results

Physical setting, water mass distributions, and nutrient drawdown

The 13 ASPIRE stations first opened to ≤ 50% ice cover as early as Day 255 (12 September; Sta. 57) and the average was Day 299 (26 October) ± 34 d (n = 13; Table 1). Extended ice-free (0%) conditions were observed as early as Day 318 (14 November; Sta. 13), but nearly half (6) of the 13 stations experienced ≤ 1 ice-free day before sampling (Table 1). A few of the open stations exhibited up to 4 days of 0% ice cover before the ice fully cleared, and these days were added to the total of ice-free days for those stations. Sta. 57 in the southeast, also the site near the moored trap (Figure 1), experienced the most ice-free days (43) before sampling.

The first day that ocean color was detected by satellite at any of the 13 stations (Table 1) was Day 330 (26 November; Sta. 50), but the average for all stations was Day 346 (12 December) ± 16 days (n = 13; Table 1), just one day before the first sampling date of ASPIRE. Thus, the ASPIRE field effort occurred during the initial stages of the spring/summer bloom.

Ice concentrations at the time of sampling for the 13 stations (Table 1) ranged from 0% (for the 7 central polynya stations) to 85% (Sta. 66, in the marginal ice zone to the north of the central polynya). *Open water duration* (OWD) prior to sampling ranged from 8 to 61 d (Table 1), with an uncertainty that ranged from 8 to 22 days, and an average of 33 ± 18 days (n = 13). *Bloom spin up* time was quite variable, ranging from 0

to 74 days (average = 49 ± 25 days, n = 13) and *bloom duration* varied between 0 and 33 days (average = 14 ± 13 days; Table 1).

During ASPIRE sampling, surface pCO_2 at all 13 stations was always undersaturated with respect to the atmosphere (Table 1; see also Mu et al., 2014), ranging from 167 to 358 µatm. Thus, gas exchange at all 13 stations was always into the ocean at a rate that ranged from 4 to 49 mmol C m^{-2} d^{-1} (Table 1; average = 32 ± 14 mmol C m^{-2} d^{-1}).

Unmodified Winter Water (WW; θ ~ –1.75°C, S > 34.1; see also Randall-Goodwin et al., 2015) was not observed in the upper 100 m at these 13 stations (Figure 2), as it tended to be found between 200 and 400 m. Temperature-salinity profiles for the upper 100 m of the 13 stations (Figure 2) showed variable extents of warming and freshening of the upper portions of the WW layer through mixing with Antarctic Surface Water (AASW), but also sometimes showed the influence of heat and salt from mCDW at depth.

Potential temperatures in the upper 100 m ranged from –1.79 to –0.13°C (Figure 2), with an average of –1.31 ± 0.46 (n = 86). At 100 m, the average θ was –1.63 ± 0.15 (n = 13), which was warmer than canonical WW (θ < –1.75°C) or the observed minimum potential temperature (T_{min}) for the full water column (which ranged from –1.82 at Stations 6, 29, and 66 in the northwest to –1.41°C at Sta. 57; with a median of –1.80; n = 13; Figure 2). At the surface, potential temperature was greater, ranging from –1.47 to –0.13°C, with warmer surface waters associated with increased open water duration, ice-free shallow-stratified conditions, and sufficient time to be warmed by solar irradiation (Figure 2). The warmest surface waters were found at Sta. 35 and 48 in the upper 10 m (Figure 2). Sta. 57 was ice-free the longest (43 days; Table 1) and its summer mixed layer was the deepest (81 m; Table 1), presumably because of longer exposure to winds; it was also where a large iceberg (with an estimated keel depth of 340–450 m) was observed (see Randall-Goodwin et al., 2015). Sta. 13 also experienced a long OWD (56 days) and had a relatively deep mixed layer (42 m; Table 1). The depth of the minimum potential temperature in the upper 100 m (T_{min_100}) ranged from 28 to 100 m (Table 1). Eight stations (5, 6, 13, 18, 25, 34, 35) exhibited a subsurface heat contribution from mCDW in the upper 100 m (Figure 2; black lines).

Salinity in the upper 100 m ranged between 33.5 and 34.1 (Figure 2), with an average of 33.95 ± 0.11 (n = 86), and all but three samples had S > 33.7. Surface salinity was reduced relative to deeper waters at all open water stations we sampled, indicating that ice melt had already freshened the upper layer (see Randall-Goodwin et al., 2015). Salinity was especially reduced at the near surface for two of the partially sea ice-covered stations (Sta. 66 at 85% sea ice cover, and Sta. 68 at 68% sea ice cover; Table 1; Figure 2). The salinity at 100 m depth varied across the 13 stations, from 33.9 to 34.1 (average = 34.0 ± 0.04, n = 13), and was somewhat fresher than canonical WW (S > 34.1), but also indicated variable salt contributions from deep mCDW as well (Figure 2).

As described above, T_{min_100} was found at depths < 100 m for 8 of the 13 stations (Table 1; Figure 2). Below T_{min_100}, the θ-S profile curved upward and to the right (indicating additions of heat and salt), i.e., toward the mCDW end member (black line segments on Figure 2). Surface mixed layer depths ranged from 10 to 81 m (average = 25 ± 19 m, n = 13; Table 1), with the deepest value seen at Sta. 57.

All samples of unmodified WW collected during ASPIRE (entirely from depths below 100 m; n = 19) gave fairly narrow ranges for inorganic and organic concentrations (± < 5%; Table 2). The same analysis for the samples of mCDW (S > 34.5; depth > 400 m; n = 41) resulted in much higher variability (> 20% in some measures; Table 2), perhaps reflecting different degrees of modification from the ice shelf or interaction with the seafloor sediments. Inorganic nutrients and carbon were higher in the deeper, warmer, saltier mCDW than in WW, although disproportionately so: DIN and DIP were ~10% higher; $Si(OH)_4$, ~18% higher; and DIC, ~2% higher. Dissolved oxygen (DO) was significantly lower (32%) in mCDW (Table 2; Figure 2). The average concentrations of POC and PN for either water mass were not significantly different from zero (given measurement blanks), but could be high in some samples. In contrast, the DOC concentrations in both WW and mCDW, 69 ± 9.6 µmol C L^{-1} and 76 ± 18 µmol C L^{-1}, respectively, were unexpectedly high, especially in near-bottom waters (up to 118 µmol C L^{-1}). DON in WW (3.0 ± 2.4 µmol N L^{-1}) was similar to that in mCDW (2.6 ± 1.5 µmol N L^{-1}).

In the upper water column of the ASP, the DIN was dominated by nitrate. Ammonium was always < 2 µmol L^{-1}, and typically < 1 µmol L^{-1} except for three sample depths (10, 25, and 40 m) at Sta. 66 (1.3-1.6 µmol L^{-1}; where significant abundances of ice krill were found; see Wilson et al., 2015) and for one sample (85 m) at Sta. 48 (1.2 µmol L^{-1}). Nitrite was always < 0.14 µmol N L^{-1}. Nitrate concentrations in the upper 100 m ranged from 7.2 to 31.7 µmol L^{-1}. At the 13 stations, deep (100 m) values for DIN were variable and ranged from 28.4 to 31.7 µmol N L^{-1} (average = 29.8 ± 0.88; n = 13), which were slightly lower on average than, but not significantly different from, the independently determined WW end member (Table 2) described above. Concentrations of DIN at T_{min_100}, were slightly lower (average = 29.2 ± 1.35; minimum = 26.9; n = 13) than at 100 m (29.8 ± 0.91; minimum = 28.4; n = 13), illustrating the variable influence of deep mCDW.

Table 2. Water mass endmembers

Parameter	AASW[a] (0–100 m)		WW[b] ± 1 S.D. (n = 19)	mCDW[c] ± 1 S.D. (n = 41)
	Lower value	Upper value		
Temperature (°C)	–1.79	–0.13	–1.79 ± 0.02	+0.70 ± 0.22
Salinity	33.5	34.1	34.13 ± 0.01	34.60 ± 0.070
DIN (μmol N L^{-1})	7.31	31.84	30.88 ± 0.51	33.45 ± 0.59
HPO_4^{2-} (μmol P L^{-1})	0.63	2.1	1.95 ± 0.05	2.14 ± 0.05
$Si(OH)_4$	64	99	91.5 ± 4.6	106.7 ± 4.09
dFe (nmol kg^{-1})[d]	0.06	0.8	0.3 ± 0.05	0.37 ± 0.05
DIC (μmol C L^{-1})	2094	2273	2276 ± 5	2320 ± 3
ALK (μmol C L^{-1})	2225	2377	2358 ± 6	2378 ± 37
DIC (μmol C kg^{-1})	2038	2213	2215 ± 5	2257 ± 3
ALK (μmol C kg^{-1})	2166	2314	2295 ± 5	2314 ± 36
DO (μmol O_2 L^{-1})	284	465	287 ± 4.8	196 ± 2.9
POC (μmol C L^{-1})	nd[e]	78	0.013 ± 0.02	0.33 ± 0.37
PN (μmol N L^{-1})	nd	12	0.004 ± 0.005	0.03 ± 0.05
DOC (μmol C L^{-1})	53	127	69 ± 9.6	76 ± 18
DON (μmol N L^{-1})	nd	8.5	3.0 ± 2.4	2.6 ± 1.5

[a]Antarctic Surface Water
[b]Winter Water, defined by all ASPIRE samples where θ < –1.75°C and S > 34.1
[c]Modified Circumpolar Deep Water (mCDW), defined by all ASPIRE samples where S > 34.5 and depth > 400 m
[d]From Sherrell et al. (2015)
[e]Not detected

doi: 10.12952/journal.elementa.000140.t002

The estimates of integrated nitrogen drawdown (ΔDIN) ranged from 27 to 740 mmol N m^{-2} (Table 1; Figure 4). Plotted against station rank, the increase in ΔDIN was nearly linear (R^2 = 0.98; Figure 4), confirming that even though we did not sample a true time series, ASPIRE stations can be rearranged to represent a full range of bloom conditions. Two small breaks in slope (Figure 4) suggest that the stations can be grouped into early bloom (Stations 5, 68, 6, 34, and 66), mid-bloom (Stations 18, 13, and 25), and high bloom (Stations 50, 35, 48, 29, 57) phases. The five early blooms stations were also the westernmost stations (Figure 4). The high bloom stations tended to be observed later in the expedition compared to mid-bloom stations, and toward the south and east (Stations 35, 48, 29, 57), where the polynya was open longer (Table 1; Figure 4).

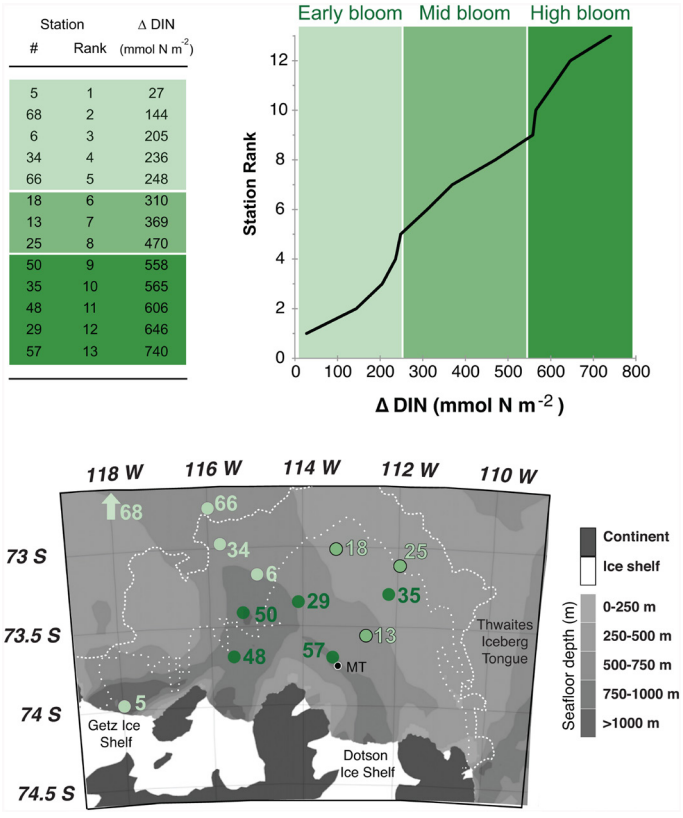

Figure 4
Station classifications.

The ranking and spatial arrangement of stations is compared according to increasing ΔDIN (mmol N m^{-2}, as listed in Table 1). The increase in ΔDIN over station rank is linear (R^2 = 0.98), with small breaks in slope near 250 and 550 mmol N m^{-2}. One possible grouping of stations, therefore, is: 1) early bloom stations (light green) indicated by ΔDIN < 250 mmol N m^{-2}; 2) mid-bloom stations (medium green) indicated by 250 < ΔDIN < 550 mmol N m^{-2}, and 3) high bloom stations (dark green) indicated by ΔDIN > 550 mmol N m^{-2}. Geographic map shows that light green stations (early bloom) are located in the northern and western regions of the study area (68 is off the map, see Figure 1), medium green stations (mid-bloom) tend towards the northeast, dark green stations (high bloom) are central and southern. The white lines indicate the edge of the open water (see Mu et al., 2014) on 19 November 2010 (dotted) and 2 January 2011 (dashed), showing how the northern stations experienced fewer ice-free days.

doi: 10.12952/journal.elementa.000140.f004

Across the 13 stations, ΔDIN correlated significantly with several of the ice and bloom timing variables (Table 1; $p < 0.01$, $n = 13$), most strongly and positively with the number of ice-free days ($R = 0.87$), and inversely with the first day of extended ice-free conditions ($R = -0.85$). It also correlated significantly ($p < 0.01$) with bloom duration ($R = 0.83$), open water duration ($R = 0.80$; Figure 5A), the first day of increasing ocean color ($R = -0.74$), and ice concentration at the time of sampling ($R = -0.68$). Surface pCO_2 correlated significantly with ΔDIN ($R = -0.71$, $n = 12$, $p < 0.01$) when deeply-mixed Sta. 57 was removed from the analysis (Table 1).

As inferred above from the station groupings (Figure 4), the variation in ΔDIN also exhibited some geographic sensitivity, correlating significantly ($R = 0.63$, $p < 0.05$) with longitude (tending to be higher in the east, which was also where the sea ice disappeared first). Because spatially heterogeneous sea ice conditions explain a larger fraction of the variability in ΔDIN than geography, however, geographic transects through the polynya seem less informative than arranging the stations in terms of either sea ice timing or the integrated nitrate drawdown. All results are thus presented within the framework of increasing ΔDIN as representative of the increasing polynya opening and the subsequent algal bloom.

When stations are arranged according to ΔDIN, physical controls on the bloom progression can be observed (Figure 5). First, as mentioned above, a clear relationship exists between increasing OWD and ΔDIN (Figure 5A). Exceptions to the trend include Sta. 5 near the Getz Ice Shelf, and Sta. 13; both had relatively long OWD compared to their early or mid-bloom stages. Hydrography at these two stations indicates less warming or freshening at the surface (Figures 2, 5B, 5C), perhaps because of fewer actual ice-free days (in the case of Sta. 5; Table 1), or deeper wind mixing (in the case of Sta. 13; Table 1).

The progressive warming and freshening in the polynya surface waters during the bloom progression is observed when comparing temperature and salinity profiles against ΔDIN (Figure 5B, 5C). At early bloom stations, the upper water column is mostly cold (< –1.4 °C; Figure 5B) with surface freshening at some stations (Figure 5C). Later in the bloom progression, warmth penetrates increasingly deeper into the water column through the mid-bloom and then surface temperatures peak during high bloom. Warming was seen penetrating deeper waters at several stations, particularly Stations 13 (to 60 m), 35 and 50 (to 90 m), 29 (to 80 m), and 57 (to 100 m). Freshening from the surface down to the deeper depths corresponded with those stations that indicated downward mixing of surface heat (Figure 5C), and suggesting local mixing events.

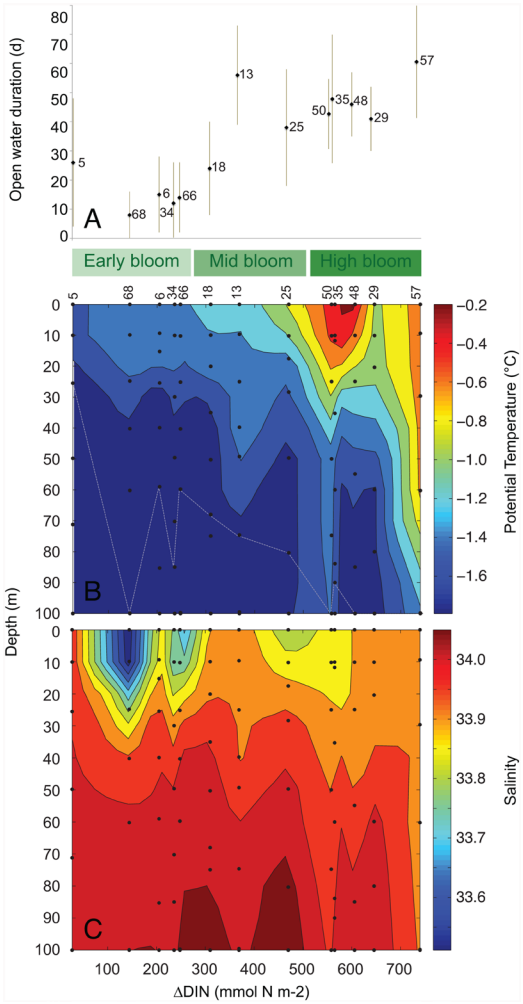

Figure 5

Hydrography of the 13 ASP stations examined.

Physical characteristics of the 13 stations examined against increasing integrated nitrate depletion (ΔDIN, mmol N m^{-2}) and bloom stage (green scale as in Figure 4). A) open water duration (days) for each station (numbered); (B) potential temperature (°C; colored according to legend) profiles contoured with increasing ΔDIN, with the white dotted line indicating the depth of integration for each station; (C) salinity profiles contoured versus ΔDIN. Actual measurements indicated by black data points.

doi: 10.12952/journal.elementa.000140.f005

Inorganic carbon and nutrients

Inorganic carbon and nutrients were higher and well mixed at early bloom stations such as Stations 5 and 68, but then DIC, DIN, and DIP decreased proportionally, starting near the surface and moving to depth with increasing ΔDIN (Figure 6A, B, C). An exception was Sta. 57 (and to some extent Sta. 13), which suggested deep mixing, as described above for θ and S. Concentrations of DIC (reported here in μmol L^{-1} for comparison to N and P) ranged from a high of 2273 μmol C L^{-1} (2213 μmol kg^{-1}) in the deeper waters, to a low of 2094 μmol C L^{-1} (2038 μmol kg^{-1}) in the near surface waters of Sta. 35 (Figure 6A). Concentrations of DIN ranged from 7.31 to 31.84 μmol N L^{-1}, with the highest values found at Sta. 5 and in the deeper waters of most stations (Figure 6B) and the lowest concentrations (< 10 μmol N L^{-1}) in the surface or near-surface waters at high bloom stations. The sample-by-sample concentrations of DIN correlated very well with those of DIC ($R = 0.99$, $n = 42$, $p < 0.01$). Concentrations of DIP ranged from 0.63 to 2.1 μmol P L^{-1} (Figure 6C) and also correlated very well with DIC ($R = 0.99$, $n = 42$, $p < 0.01$) and DIN ($R = 0.99$, $n = 81$, $p < 0.01$).

Integrated water column ΔDIC and ΔDIP (Table 3) corresponded very well ($R = 0.98$; $n = 7$ and 13, respectively; $p < 0.01$) with integrated ΔDIN calculations. Average stoichiometric ratios for the region (ΔDIC:ΔDIP = 123 ± 45; ΔDIN:ΔDIP = 16.8 ± 2.2; ΔDIC:ΔDIN = 6.6 ± 0.89; $n = 29$; Table 3) were not significantly different ($p > 0.05$) from average living marine plankton (C:N:P = 106:16:1; Redfield et al., 1963). Stoichiometry did not correspond well with bloom stage. Stations 66, 25, 50, and 35 all exhibited ΔDIC:ΔDIP = 104-125, whereas Stations 13 and 57 both had lower values at 90-97. Sta. 5, with ΔDIC:ΔDIP = 221, was an outlier, suggesting that the biological signal was too small to get a good ratio.

Concentrations of $Si(OH)_4$ in the upper 100 m ranged from 64 to 99 μmol Si L^{-1} with an average value of 85 ± 8 μmol Si L^{-1} (data not shown). The concentrations at 100 m (average = 89 ± 7 μmol Si L^{-1}) were generally lower than but not significantly different from the WW endmember (91.5 ± 0.05 μmol Si L^{-1}). With this large observed variability, there may have been a problem with consistency of the daily $Si(OH)_4$ standard curve on board ship, and concentration data are not comparable from station to station. All samples from a single profile were run on the same day with the same standards, however. Thus, for any given station,

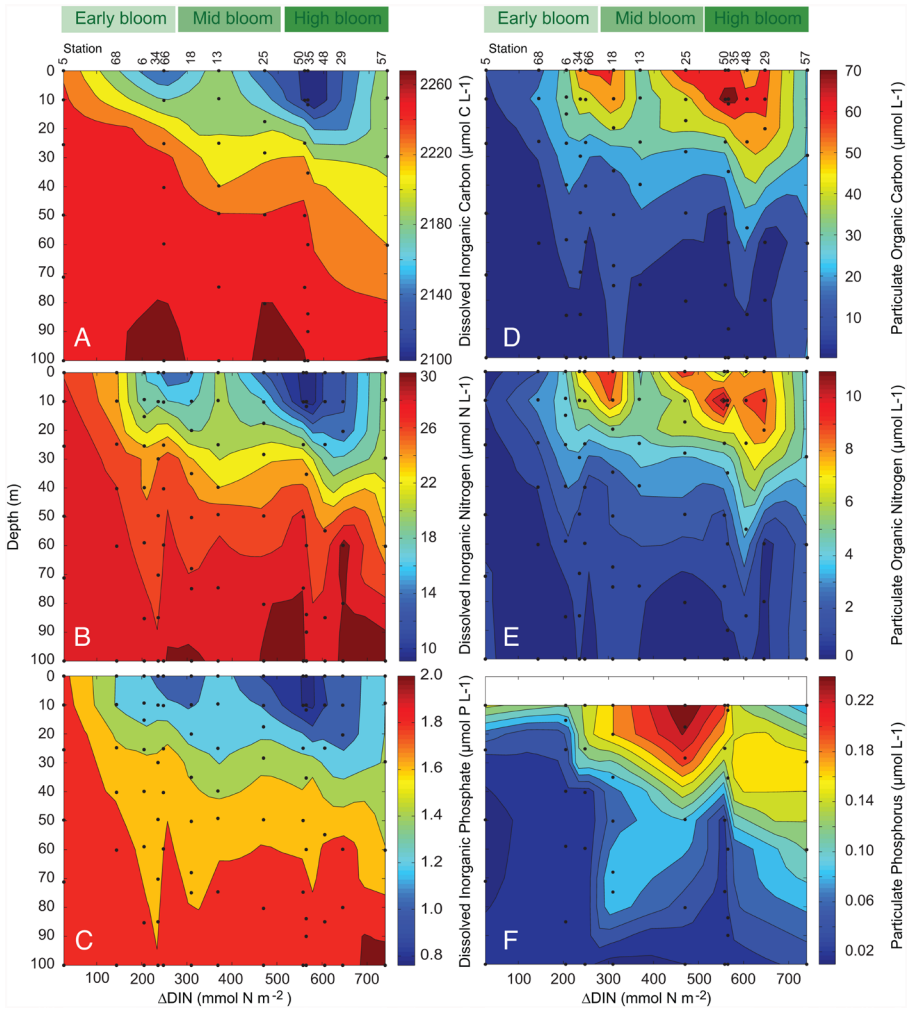

Figure 6

Carbon, nitrogen, and phosphorus inventories in the ASP.

Inventory profiles for the 13 stations contoured against increasing nitrate depletion (ΔDIN; mmol N m^{-2}) and bloom stage (green scale as in Figure 4). (A) dissolved inorganic carbon (DIC, μmol C L^{-1}); (B) dissolved inorganic nitrogen (DIN, μmol N L^{-1}); (C) dissolved inorganic phosphorus (DIP, μmol P L^{-1}); (D) particulate organic carbon (POC, μmol C L^{-1}); (E) particulate organic nitrogen (PN, μmol N L^{-1}); and (F) particulate phosphorus (PP, μmol P L^{-1}). The left and right columns are independently measured, so the coherence is notable. Samples for PP came from separate TMC-CTD casts and there were fewer profiles available.

doi: 10.12952/journal.elementa.000140.f006

Table 3. Integrated net changes in inorganic carbon and nutrients, with stoichiometric ratios, over the upper water column[a]

Station grouping[b]	Station #	Event #	Changing integrated inventories				Stoichiometric ratios					
			ΔDIN (mmol N m^{-2})	ΔDIC (mmol C m^{-2})	ΔDIP (mmolP m^{-2})	ΔSi (mmol Si m^{-2})	ΔDIC: ΔDIP	ΔDIC: ΔDIN	ΔDIN: ΔDIP	ΔDIC: ΔSi	ΔSi: ΔDIN	ΔSi: ΔDIP
Early bloom	5	5.04	27	213	1	9	221	8.0	28	24.3	0.3	9.1
	68	68.01	144	-	14	333	-	-	11	-	2.3	24
	6	6.03	205	-	11	11	-	-	19	-	0.1	1.0
	34	34.03	236	-	14	36	-	-	17	-	0.2	2.6
	66	66.02	248	1568	15	141	107	6.3	17	11.1	0.6	10
Mid-bloom	18	18.01	310	-	18	79	-	-	18	-	0.3	4.5
	13	13.08	369	1921	21	296	90	5.2	17	6.5	0.8	14
	25	25.02	470	2917	28	(–185)[e]	104	6.2	17	(–15.8)[e]	(–0.4)[e]	(–6.6)[e]
High bloom	50	50.09	558	3736	31	223	121	6.7	18	16.8	0.4	7.2
	35	35.11	565	4178	34	489	125	7.4	17	8.5	0.9	15
	48	48.02	606	-	34	54	-	-	18	-	0.1	1.6
	29	29.02	646	-	35	513	-	-	18	-	0.8	15
	57	57.11	740	4711	49	698	97	6.4	15	6.8	0.9	14
All stations	$R_{\Delta DIN}$[c]	-[d]	**1.00**	**0.98**	**0.98**	**0.68**	**–0.69**	–0.31	–0.28	–0.66	–0.03	0.07
	AVE[c]	-	-	-	-	-	123	6.6	16.8	12.3	0.63	9.8
	S.D.	-	-	-	-	-	45	0.89	2.2	7.0	0.62	6.9
	n	-	-	-	-	-	7	7	13	6	12	12

[a]Integrated to T_{min_100}, arranged in order of increasing nitrogen drawdown (ΔDIN)
[b]By bloom stage, as shown in Figure 4
[c]Including polynya-wide averages of stoichiometric ratios, with standard deviation (S.D.) and *n* value, and correlation (*R*) of each variable with ΔDIN (significant correlations: $p < 0.01$ in bold)
[d]Indicates not applicable or not available
[e]Negative value not included in average or correlation
doi: 10.12952/journal.elementa.000140.t003

the silicate drawdown (ΔSi; Figure 7) is the better way to examine the data because it shows vertical gradients that depend less on a consistent daily standard curve. Although the $\Delta Si(OH)_4$ data indicate surface depletion at some stations, the silicate depletion did not follow the ΔDIN as well as the other nutrients did (R = 0.68, $p < 0.01$, n = 12). Integrated ΔSi ranged from 9 to 700 mmol Si m^{-2} (Table 3), except for a negative value at one station (Sta. 25) that suggested a deep source or dissolution of advected particulate silicate. The ΔDIC: ΔSi ratio (Table 3) varied widely but the average (when the one negative value was removed) was higher but not significantly different (average = 12.3 ± 7, n = 6) from the typical ratio for diatoms (7.1; Brzezinski, 1985). The ΔSi:ΔDIP and ΔSi:ΔDIN ratios (Table 3) were also highly variable and generally lower on average (9.8 ± 7, 0.63 ± 0.62, respectively; n = 12) than typical for diatoms (15 and 0.94, respectively; Brzezinski, 1985), indicating the presence of other phytoplankton groups.

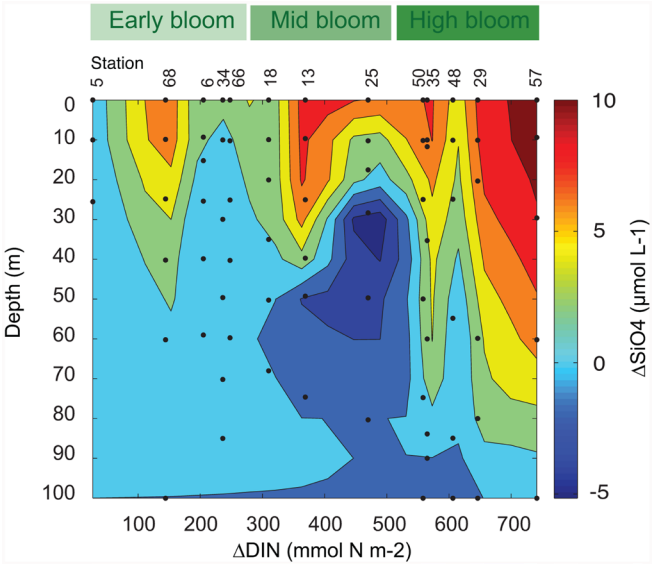

Figure 7
Silicate drawdown in the ASP.

Dissolved silicate drawdown (ΔSi_{bio}, µmol C L^{-1}) profiled for the 13 stations contoured against increasing nitrate depletion (ΔDIN, mmol N m^{-2}) and bloom stage (green scale as in Figure 4). The partial coherence with Figure 6 is notable.

doi: 10.12952/journal.elementa.000140.f007

Particulate organic matter

The buildup of particulate organic matter mirrored the drawdown of inorganic nutrients as ΔDIN increased from station to station (Figure 6). Concentrations of POC ranged from not detectable to 78 μmol C L^{-1} with highest values in the upper 20 m at stations with higher ΔDIN (Figure 6D). The buildup of POC accounted for 49-98% of the inorganic carbon drawdown (ΔDIC), with an average of 75 ± 19% ($n = 7$). Concentrations of PN (Figure 6E) ranged from not detectable to 12 μmol N L^{-1} and showed similar distribution as POC ($R = 0.98$, $n = 79$, $p < 0.01$), with sample-by-sample POC:PN values averaging 7.1 ± 2.1 ($n = 64$). Concentrations of PP (from the TMC CTD cast, data only available = 10 m; Figure 6F) correlated significantly with POC and PN ($R = 0.61$ and 0.64, respectively; $n = 42$; $p < 0.01$). Notable deviations occurred in the 10-30 m depths of Sta. 25 where PP was high, but POC and PN were less so.

Across the region, the stoichiometric ratios for particle samples in the upper water column (0-100 m; POC:PP = 279 ± 176; POC:PN = 7.4 ± 4.0; PN:PP = 40 ± 25; $n = 64$ for POC:PN and $n = 31$ for PP) were much more variable than the dissolved inorganic ratios, and tended to be poor in phosphorus, but, with the high variances, were not significantly different ($p > 0.05$) from typical values for living plankton (C:P = 106, C:N = 6.6; N:P = 16; Redfield et al., 1963). The large variance suggests some preferential remineralization of P and N (relative to C) at some but not all stations and depths.

Integrated water column ΔPOC and ΔPN values for each station (Table 4) ranged from 180 to 3229 mmol C m^{-2} and 20 to 500 mmol N m^{-2}, respectively, and correlated significantly with each other ($R = 0.96$, $n = 13$, $p < 0.01$) and with ΔDIN ($R = 0.82$ and 0.81, respectively; $n = 13$; $p < 0.01$). With the large maximum at Sta. 25, integrated ΔPP by station (ranging from 2.8 to 17 mmol P m^{-2}) did not correlate significantly with ΔPOC ($R = 0.62$, n = 8, $p > 0.05$) but was better correlated with ΔPN and ΔDIN ($R = 0.70$, 0.72, respectively; $n = 8$; $p < 0.05$). Stoichiometric ratios based on integrated values for each station (Table 4; ΔPOC:ΔPP = 230 ± 63; ΔPN:ΔPP = 33 ± 7.8; ΔPOC:ΔPN = 7.0 ± 0.8) were similar to those described above for individual depths, but less variable, distinguishing them better from the Redfield ratios for living plankton. The lower P content of particles in the upper 100 m persisted relative to changes in inorganic inventories (Table 4), again suggesting some preferential remineralization of phosphorus.

Dissolved organic matter

The balance of DOM sources and sinks in the ASP, as represented by the observed inventories, appear to be more complex than for POM and nutrients in that they do not follow the bloom progression as well. Generally, DOC and DON concentrations were higher in surface waters relative to subsurface (Figure 8), but they did not exhibit the characteristic surface build up or progressive deepening with ΔDIN or bloom stage that was observed with POC and PN. Concentrations of DOC in the upper water column ranged from

Table 4. Integrated changes in particulate and dissolved organic matter and their ratios over the upper water column[a]

Station grouping[b]	Station #[c]	ΔDIN (mmol N m^{-2}	ΔPOC (mmol C m^{-2})	ΔPN (mmol N m^{-2})	ΔPP (mmol P m^{-2})	ΔPOC: ΔPP	ΔPOC: ΔPN	ΔPN: ΔPP	ΔDOC (mmol C m^{-2})	ΔDON (mmol N m^{-2})	ΔDOC: ΔDON
Early bloom	5	27	180	20	2.8	63	9.0	7	(–38)	1	-
	68	144	707	110	-	-	6.4	-	(–144)	(–46)	3.1
	6	205	1564	217	3.3	468	7.2	65	750	66	11
	34	236	1981	290	-	-	6.8	-	(–86)	39	-
	66	248	1537	208	5.5	279	7.4	38	403	(–10)	-
Mid-bloom	18	310	2026	304	8.3	244	6.7	37	895	34	26
	13	369	1873	263	-	-	7.1	-	265	84	3.1
	25	470	1977	310	17.0	116	6.4	18	1130	103	11
High bloom	50	558	2234	348	8.8	254	6.4	40	1210	(–100)	-
	35	565	2799	338	9.9	284	8.3	34	1390	8	175
	48	606	3229	500	-	-	6.5	-	(–1110)	118	-
	29	646	2766	404	-	-	6.9	-	(–180)	107	-
	57	740	2291	358	11.4	201	6.4	31	(–215)	70	-
All stations	$R_{\Delta DIN}$[c]	**1.00**	**0.86**	**0.87**	0.72*	0.01	–0.43	0.08	–0.27	0.33	0.69
	AVE[c]	-[d]	-	-	-	230	7.0	33	-	-	38
	S.D.	-	-	-	-	63	0.81	7.8	-	-	67
	n	-	-	-	-	8	13	8	-	-	6

[a]Integrated to T_{min_100}, arranged in order of increasing nitrogen drawdown (ΔDIN)
[b]By bloom stage, as shown in Figure 4
[c]Including polynya-wide averages, with standard deviation (S.D.) and *n* value, and correlation (*R*) of each variable with ΔDIN (significant correlations: $p < 0.01$ in bold, $p < 0.05$ with asterisk)
[d]Indicates not applicable or not available

doi: 10.12952/journal.elementa.000140.t004

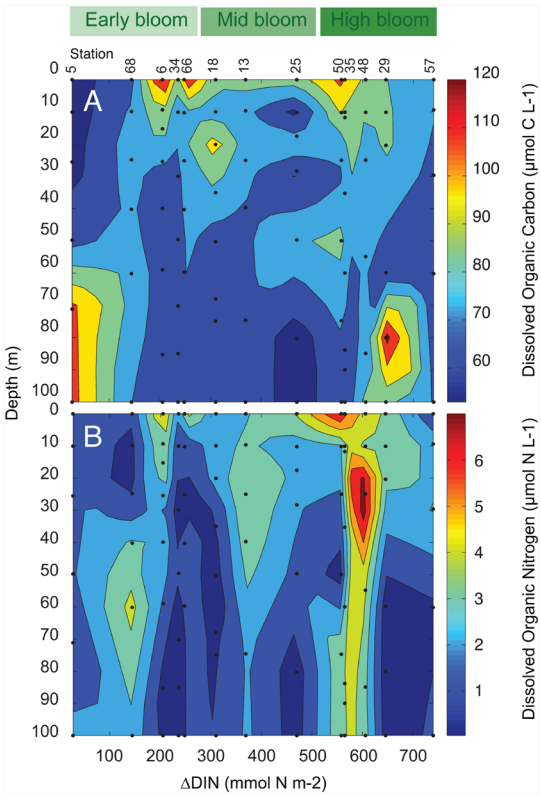

Figure 8

Dissolved organic carbon and nitrogen inventories in the ASP.

Dissolved organic inventory profiles for the 13 stations contoured against increasing nitrate depletion (ΔDIN, mmol N m^{-2}) and bloom stage (green scale as in Figure 4). A) dissolved organic carbon (DOC, µmol C L^{-1}); and (B) dissolved organic nitrogen (DON, µmol N L^{-1}). The lack of coherence with Figure 6 is notable.

doi: 10.12952/journal.elementa.000140.f008

53 to 127 µmol L^{-1}, with peak values at the surface of early bloom Stations 6 and 66 (Figure 8A), which were both in the marginal ice zone at the time of sampling. Although typical melting sea ice contributions were accounted for in the mixing model, the biomass and algal productivity in sea ice can be extremely heterogeneous, and inputs to the ocean from any given melt could vary substantially. A few deeper samples also exhibited relatively high concentrations (Sta. 5, 80-100 m; Sta. 29, 80 m; Sta. 48, 100 m), suggesting variable subsurface sources of DOC to the water column (contamination was ruled out because the DON for those same samples was low).

Concentrations of DON ranged from not detected to 8.5 µmol L^{-1} (Figure 8B), with some high concentrations in the surface and subsurface at higher ΔDIN stations (e.g., Stations 35 and 48). The correlation between sample DOC and DON concentrations was weak but significant for all samples in the upper 100 m ($R = 0.39$, $n = 80$, $p < 0.01$), with a carbon-rich average DOC:DON ratio of 47 ± 38 ($n = 80$). The C:N ratio dropped to a mean of 23 ± 35 if we subtracted a canonical Southern Ocean deepwater DOC value of 45 µmol L^{-1} from the measured DOC and recalculated the ratio (because we observed DON = 0, we did not subtract a deepwater DON). The average DOC value at T_{min_100} (69 ± 10 µmol C L^{-1}) had a large range, but matched the WW average and range very well. The average DON at T_{min_100} (1.9 ± 1.5 µmol N L^{-1}, $n = 13$) was a bit lower, but not significantly different from that of WW or from zero.

Integrated ΔDOC values (Table 4) ranged from large and positive (1390 mmol C m^{-2} at Sta. 35) to unexpectedly large and negative (–1110 mmol C m^{-2} at Sta. 48), and they did not correlate significantly with ΔDIN or correspond with bloom stage. Integrated ΔDON also ranged from large and positive (118 mmol N m^{-2} at Sta. 48) to large and negative (–100 at Sta. 50). The ΔDOC:ΔDON ratio (only calculated when both ΔDOC and ΔDON were the same sign) also varied widely (ranging from 3 to 170; Table 4). These outcomes were driven at least in part by the variability of DOC and DON at T_{min_100} and the high sensitivity of the mixing model and integration calculations to small differences in concentration.

Biomass in the upper 100 m

All biomass stocks except mesozooplankton generally exhibited their highest accumulations in the high bloom regions with higher ΔDIN (Figure 9), although most did not have significant correlations with ΔDIN (Table 5). Chlorophyll *a* concentrations (Figure 9A) ranged from 0.02 to 22 µg Chl *a* L^{-1}, were highest within the surface or near-surface waters of the central polynya, and exhibited an integrated buildup that ranged from 74 to 828 mg m^{-2} (average = 613 ± 147 mg m^{-2}; Table 5) and correlated well with ΔDIN ($R = 0.68$, $n = 13$, $p < 0.01$; Figure 9A). A subsurface (10-20 m) Chl *a* maximum was observed at several mid- or high bloom stations (Stations 18, 50, 48, 35, and 29). Concentrations of Chl *a* correlated positively with POC concentrations on individual samples ($R = 0.90$, $n = 79$, $p < 0.01$), with the POC:Chl *a* ratio ranging

Table 5. Integrated biomass inventories and changes over the upper water column[a]

Station grouping[b]	Station #[c]	Chl *a* (mg m^{-2}, A)	ΔPOC (B)	C:Chl *a* (w/w, [Bx12]/A)	ΔBAC (C)	ΔHNAN (D)	ΔDINO (E)	ΔCIL (F)	ΔZOOP		Algal C (G=A–C–D–E–F)	Algal C:Chl *a* (w/w, Gx12/A)
									Day	Night		
Early bloom	5	177	608	41	59	1.1	-	-	-	-	-	-
	68	74	707	115	-[d]	1.6	68	45	0.014	0.036	590	96
	6	552	1963	43	36	2.6	-	-	-	-	-	-
	34	679	2100	37	53	1.9	101	28	-	-	1920	34
	66	350	1730	59	67	4.4	122	48	-	-	1490	51
Mid-bloom	18	662	2430	44	82	2.1	-	-	-	-	-	-
	13	622	2060	40	51	1.0	82	6	0.047	0.169	1920	37
	25	502	1980	47	61	1.6	91	24	0.016	0.023	1800	43
High bloom	50	436	2230	62	58	2.9	178	43	0.035	0.066	1950	54
	35	601	2860	57	50	3.0	31[e]	5[e]	0.018	0.027	2770	-
	48	828	3230	47	81	3.4	181	91	-	-	2870	42
	29	762	2770	44	36	3.1	-	-	-	-	-	-
	57	690	2290	40	123	1.8	89	66	0.016	0.010	2010	35
All stations	$R_{\Delta DIN}$[c]	**0.68**	**0.79**	–0.24	0.48	0.30	0.21	0.31	–0.07	–0.32	**0.72**	–0.52

[a]Integrated biomass (mmol C m^{-2}, except where noted) to 100 m, arranged in order of increasing nitrogen drawdown (ΔDIN)
[b]By bloom stage, as shown in Figure 4
[c]Including polynya-wide correlation (*R*) of each variable with ΔDIN (significant correlations: $p < 0.01$ in bold)
[d]Indicates not available
[e]Integrated to 12 m only (no data below 12 m); not included in correlation
doi: 10.12952/journal.elementa.000140.t005

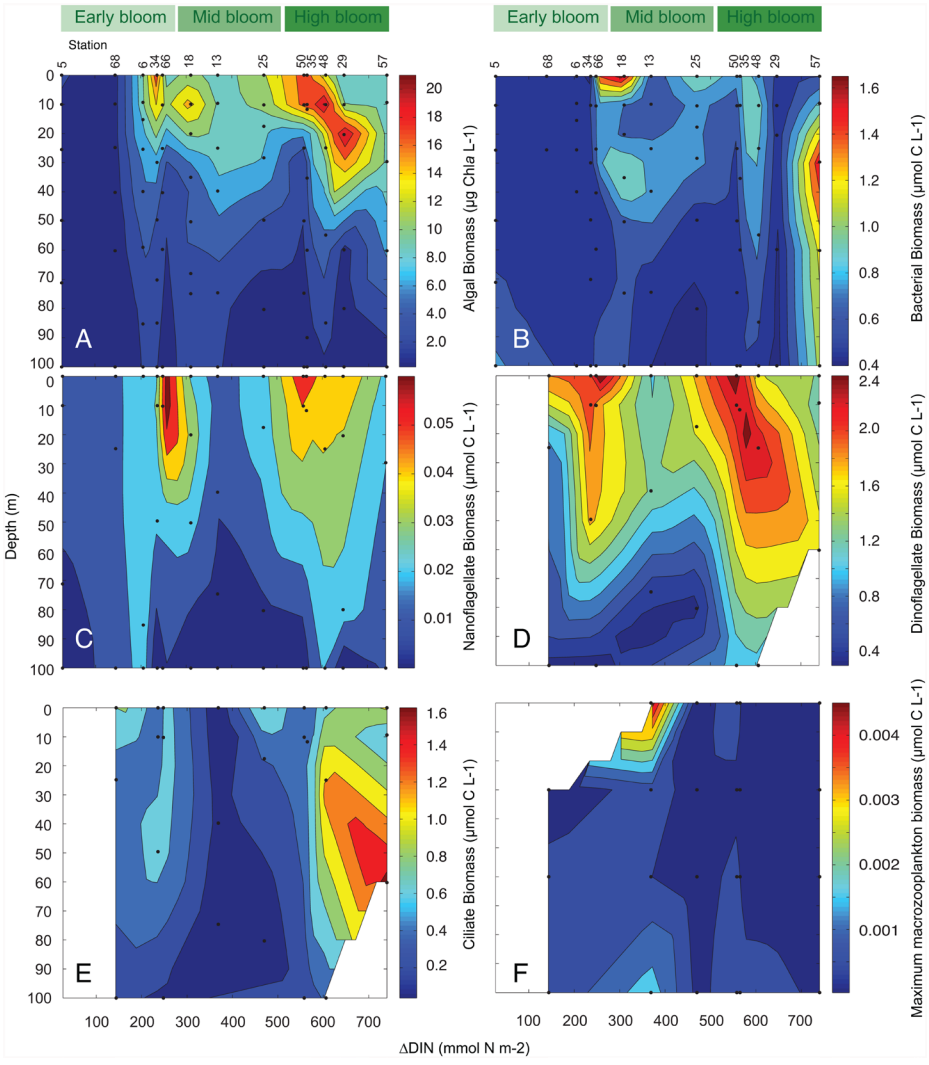

Figure 9

Biomass in the ASP.

Biomass profiles for the 13 stations contoured against increasing nitrate depletion (ΔDIN, mmol N m^{-2}) and bloom stage (green scale as in Figure 4). A) algal biomass as chlorophyll *a* concentration (µg Chl *a* L^{-1}); (B) bacterial biomass (µmol C L^{-1}); (C) nanoflagellate biomass (µmol C L^{-1}); (D) dinoflagellate biomass (µmol C L^{-1}); (E) ciliate biomass (µmol C L^{-1}); and (F) maximum zooplankton biomass (day or night, µmol C L^{-1}). Note that scales are different for each microbial contribution.

doi: 10.12952/journal.elementa.000140.f009

from 28 to 271 (median = 45; $n = 76$, excluding samples with < 0.5 µg Chl *a* L^{-1}), with higher values found in samples with 1.0-1.5 µg Chl *a* L^{-1}. Integrated ΔChl *a* also correlated significantly with ΔDIC ($R = 0.79$, n = 7, p < 0.05), as well as ΔPOC, and ΔPN ($R = 0.87$, and 0.87, respectively; $n = 13$; $p < 0.01$). Correlations improve if the same depth intervals are used (e.g., for Chl a_{100} versus ΔPOC_{100}: $R = 0.91$, $n = 13$, $p < 0.01$). Integrated ΔPOC_{100}:Chl *a* ratios (Table 5) ranged from 37 (at Sta. 34) to 115 (at the partially ice-covered Sta. 68), with a median of 44 (average = 52 ± 20, $n = 13$), but did not correlate significantly with ΔDIN ($R = -0.24$, $n = 12$, $p > 0.05$).

Phytoplankton community structure (as defined by CHEMTAX pigment analysis) was dominated (> 80%) by *Phaeocystis antarctica* at all stations except early bloom Stations 6 and 68 (Table 6), where diatoms contributed 50 and 77%, respectively, to the integrated biomass. Diatoms were otherwise a small fraction of the integrated biomass (median = 2%) at the time of sampling, and when they were found, they were usually in the deeper waters with lower Chl *a* concentration. Sample-by-sample comparison throughout the upper 100 m showed significant negative correlation ($R = -0.41$, $n = 107$, $p < 0.01$) between total Chl *a* concentration and diatom percentage, but a positive correlation ($R = 0.41$, $n = 107$, $p < 0.01$) with *Phaeocystis* percentage. Prasinophytes contributed modestly to most stations (median = 8%; up to 13% at Sta. 35), whereas dinoflagellates made minor contributions (< 1%) to most stations (median = 0.2%) except at Sta. 68 (15%). Cryptophytes were spotty, contributing 4% at Sta. 68 and 3% at Sta. 50, and were otherwise minor (median = 0.5%). Chlorophytes were similarly spotty, abundant at Sta. 66 (5%), but otherwise very minor (median = 0.0%). Prasinophytes correlated positively with Chl *a* concentration ($R = 0.36$, $n = 107$, $p < 0.01$), whereas dinoflagellates and cryptophytes correlated negatively ($R = -0.36$ and -0.25, $n = 107$, $p < 0.01$). Notably, the ratio of ΔSi to *s*NCP, which ranged from 0.01 to 0.35 (Table 6), correlated significantly with the integrated diatom contribution to the algal biomass ($R = 0.65$, $n = 12$, $p < 0.05$), although the correlation was dominated by the highest value found at Sta. 68 (and becomes insignificant when that data point is removed).

Bacterial abundance ranged from 1.8 to 8.3 x 10^8 cells L^{-1} (average = 3.4 ± 1.3 x 10^8 cells L^{-1}, $n = 72$) in the upper water column. Bacterial biomass ranged from 0.4 to 1.7 µmol C L^{-1} (average = 0.7 ± 0.3 µmol C L^{-1}, n = 72), generally showed a similar buildup in concert with increasing Chl *a* and ΔDIN (Figure 9B), and correlated significantly with Chl *a* concentrations ($R = 0.35$, $n = 72$; $p < 0.01$), but exhibited three notable maxima observed at the surface of Sta. 66 (in the marginal ice zone) and Sta. 18, and subsurface (30 m) at Sta. 57 where Chl *a* was relatively low. Bacterial biomass contributed 1–14% of the POC in the water column (average = 4 ± 3%, n = 54). Integrated over the upper 100 m, bacterial biomass (ΔBAC; Table 5) ranged from 36 to123 mmol C m^{-2} (average = 63 ± 24 mmol C m^{-2}, n = 12; Table 5), with the highest value at Sta. 57, and did not correlate significantly with ΔDIN ($R = 0.37$, $n = 12$, $p > 0.05$).

Heterotrophic nanoflagellate abundance ranged from 0.25 to 11 x 10^5 L^{-1}, with an average value of 4.8 ± 2.6 x 10^5 L^{-1} (n = 45), and had a significant correlation with Chl *a* concentration ($R = 0.71$, $n = 45$, $p < 0.01$). Biomass (Figure 9C) ranged from 0.0 to 0.07 µmol C L^{-1} (average = 0.024 ± 0.019, n = 45),

Table 6. Integrated phytoplankton composition over the upper water column[a]

Station grouping[b]	Station #[c]	Chl *a* (mg m^{-2})	*Phaeocystis* %	Diatoms %	Prasinophytes %	Dinoflagellates %	Cryptophytes %	Chlorophytes %	ΔSi:*s*NCP
Early bloom	5	177	87	5	8	0.0	0.4	0.0	0.04
	68	74	1	77	2	15	4	0.1	0.35
	6	552	45	50	3	2	0.0	0.0	0.01
	34	679	89	0.4	10	0.2	0.4	0.0	0.02
	66	350	80	12	0.3	1	2	5	0.09
Mid-bloom	18	662	88	0.0	10	0.2	1	0.0	0.04
	13	622	87	3	8	0.3	1	0.5	0.11
	25	502	89	1	10	0.0	0.2	0.0	–[d]
High bloom	50	436	83	13	0.2	1	3	0.0	0.04
	35	601	86	0.1	13	0.0	1	0.1	0.08
	48	828	91	0.0	9	0.2	0.4	0.0	0.01
	29	762	86	2	11	0.0	1	0.0	0.10
	57	690	91	2	7	0.4	0.3	0.1	0.13
All stations	$R_{\Delta DIN}$[c]	**0.68**	0.46	–0.47	0.30	–0.36	–0.20	–0.21	–0.11

[a]Based on CHEMTAX pigment distribution, integrated to 100 m, and arranged in order of increasing nitrogen drawdown (ΔDIN), with change in ratio of silicate to seasonal net community production (ΔSi:*s*NCP) also included
[b]By bloom stage, as shown in Figure 4
[c]Including polynya-wide correlation (*R*) of each variable with ΔDIN (significant correlations: $p < 0.01$ in bold)
[d]Indicates not available
doi: 10.12952/journal.elementa.000140.t006

accounting for < 1% the POC. The highest values were found near the surface waters of marginal ice zone Sta. 66, with smaller peaks at the surface of Stations 35 and 50. Integrated heterotrophic nanoflagellates (ΔHNAN) ranged from 1.0 to 4.4 mmol C m^{-2}, with an average of 2.5 ± 1.0 mmol C m^{-2} (n = 13; Table 5), and did not correlate significantly with ΔDIN ($R = 0.30$, $n = 13$, $p > 0.05$).

Heterotrophic/mixotrophic dinoflagellate abundance by microscopic counts ranged from 0.32 to 4.6 x 10^4 cells L^{-1}, with an average of 1.9 ± 0.97 cells L^{-1} ($n = 25$), and correlated significantly with Chl *a* ($R = 0.70$, $n = 24$, $p < 0.01$), but not with the CHEMTAX-designated (autotrophic) dinoflagellate contribution ($R = -0.15$, $n = 21$, $p > 0.05$) or the prasinophyte contribution ($R = 0.32$, $n = 21$, $p > 0.05$). Heterotrophic/mixotrophic dinoflagellate biomass ranged from 0.29 to 2.7 µmol C L^{-1} (Figure 9D; average = 1.6 ± 0.8, n = 25), exceeded bacterial biomass, and contributed an average of 5 ± 3% ($n = 18$; maximum = 15%) to POC. When integrated, heterotrophic/mixotrophic dinoflagellate biomass (ΔDINO) contributed up to 180 mmol C m^{-2} to the living carbon in the upper water column (Table 5). Integrated dinoflagellate biomass correlated best with the POC:PP ratio ($R = 0.92$, $n = 9$, $p < 0.01$).

Ciliate abundance ranged from 0 to 5.6 x 10^4 cell L^{-1}, with an average of 2.1 ± 1.6 x 10^4 cell L^{-1}. Biomass ranged from 0.02 to 1.7 µmol C L^{-1} (Figure 9E), with the highest values subsurface at Sta. 57, and it did not correlate significantly with Chl *a* ($R = 0.25$, n = 25, p > 0.05). Ciliates contributed 0.2–20% of the POC (median: 1.3%), with the highest percentages in deep water samples (e.g., Sta. 25 at 100 m). Integrated ciliate biomass ranged from 6 to 91 mmol C m^{-2} (ΔCIL; Table 5), with an average integrated value of 44 ± 26 mmol C m^{-2}, and it did not correlate significantly with ΔDIN ($R = 0.31$, $n = 9$, $p > 0.05$).

Mesozooplankton biomass in the upper 100 m (Figure 9F; Wilson et al., 2015) ranged from 0 to 0.005 µmol C L^{-1}, was greatest at Sta. 13 (where Chl *a* was low), and did not correlate with Chl *a* ($R = 0.08$, $n = 23$, $p > 0.05$). Nighttime biomass, which was higher than daytime biomass (except at Sta. 57), was used for budget calculations. Mesozooplankton (ΔZOOP) contributed the least amount of living carbon to the near surface (0–100 m) organic carbon inventory, with maximum integrated biomass (night or day) of ~0.17 mmol C m^{-2} (Table 5), and they did not correlate significantly with ΔDIN ($R = -0.32$, $n = 6$, $p > 0.05$).

For stations where the full suite of microbial biomass data was available, algal carbon (Algal C) was estimated by subtracting integrated bacterial and microzooplankton biomass from ΔPOC_{100} (Table 5). Algal C (which could be either diatoms or *Phaeocystis*, but did not include mixotrophic microzooplankton) accounted for 85–97% of total POC. Thus, most of the POC in the surface waters of the polynya was autotrophic. The algal C to Chl *a* ratio (w/w) was estimated to be 34–96 (average = 42 ± 8, $n = 8$) which was a bit lower and less variable, but not significantly different from the average integrated ΔPOC:Chl *a* ratio of 52 ± 20 (w/w; $n = 13$). Both numbers are comparable to values found for early season *Phaeocystis* blooms in the Ross Sea (48–64; Smith et al., 1998).

Biological rates

Measured rates of net primary production (NPP) for individual depths and stations ranged from 0.3 to 9.0 µmol C L^{-1} d^{-1} (average = 2.7 ± 2.0 µmol C L^{-1} d^{-1}; $n = 68$; Figure 10A), peaked early in the bloom progression at Sta. 34, and then were patchy or in decline as ΔDIN and Chl *a* continued to increase. Integrated NPP (Table 7) ranged from 84 to 333 mmol C m^{-2} d^{-1} (average = 228 ± 71, $n = 13$; greater than the satellite estimate; Arrigo et al., 2012; 2015) and did not correlate significantly with ΔDIN or ΔChl *a* ($R = 0.14$ and 0.50, respectively; $n = 13$; $p > 0.05$).

Total microbial community respiration rates at individual depths and stations, mostly measured in the upper 20 m, were high and of similar scale as NPP, ranging from 1.7 to 8.9 µmol C L^{-1} d^{-1} (Figure 10B). At a few stations (66 and 57) and near-surface depths, respiration rate was greater than the NPP measurements made at the same depths and stations (see also Williams et al., 2016). Because of the lack of full depth coverage, however, integrated rates were not calculated here.

Bacterial production followed the buildup of ΔDIN and Chl *a* more closely than NPP or community respiration (Figure 10C) with rates up to 0.33 µmol C L^{-1} d^{-1} (4 µg C L^{-1} d^{-1}) that exceeded those reported for the neighboring Ross Sea or any other Antarctic coastal systems (Williams et al., 2016). Bacterial production increases started shallow under the sea ice at Sta. 66 and then deepened with increasing ΔDIN and bloom stage. Integrated values (BP; Table 7) ranged from 1.8 to 18 mmol C m^{-2} d^{-1} (average = 11 ± 4.3 mmol C m^{-2} d^{-1}, $n = 13$) that correlated significantly with ΔDIN and ΔChl *a* ($R = 0.70$ and 0.75, respectively; $n = 13$; $p < 0.01$), but not bacterial biomass ($R = -0.08$, $n = 12$, $p > 0.05$). Integrated BP/NPP ratios ranged from 2 to 9% (average = 5 ± 2%, n = 13; see Williams et al., 2016).

Dinoflagellate growth in the incubations from Sta. 35 (12 m) was linear ($R^2 = 0.82$, n = 18, $p < 0.001$) over 13 days with a slope of 0.27 ± 0.069 (95% ci) µmol C L^{-1} d^{-1}, with no significant differences in slope found between the two size fractions. Dinoflagellate growth and grazing rates were calculated as 13% C d^{-1} and 43% C d^{-1}, respectively. If we apply these rates to the biomass distributions at the other stations, we cautiously estimated integrated dinoflagellate grazing rates as 30–77 mmol C m^{-2} d^{-1} in the upper 100 m, potentially accounting for 13–47% of NPP (Table 7).

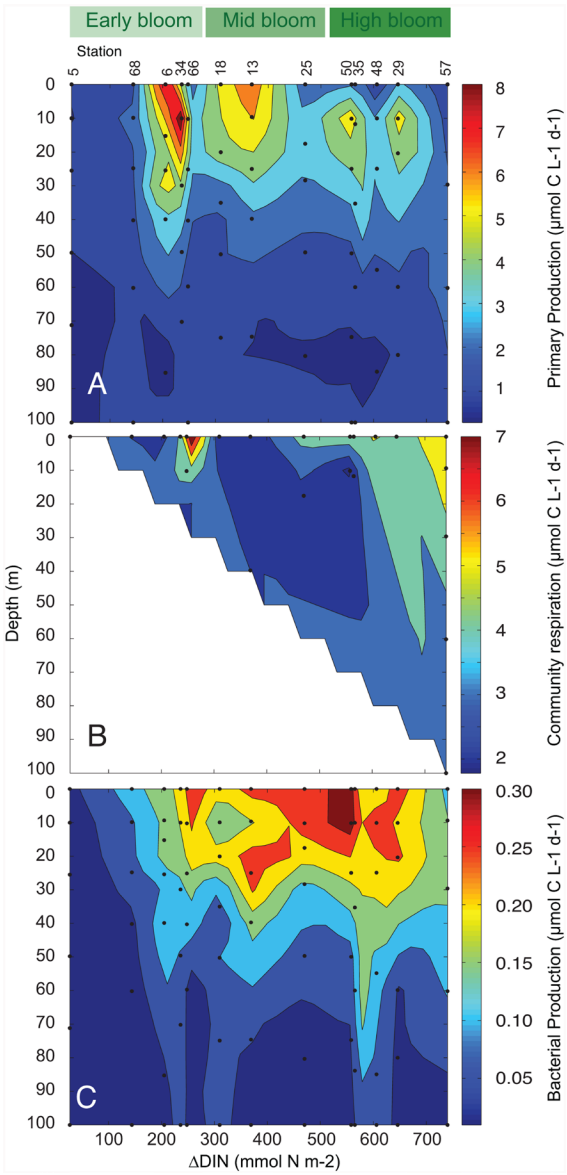

Figure 10

Production and respiration in the ASP.

Biological rate profiles for the 13 stations contoured against increasing nitrate depletion (ΔDIN, mmol N m^{-2}) and bloom stage (green scale as in Figure 4). A) net primary production (NPP, µmol C L^{-1} d^{-1}); (B) community respiration (µmol C L^{-1} d^{-1}); and (C) bacterial production (µmol C L^{-1} d^{-1}).

doi: 10.12952/journal.elementa.000140.f010

Ciliate growth in the incubations from Sta. 35 (12 m) was also linear (R^2 = 0.44, n = 17, $p < 0.05$) over 13 days with a slope of 0.033 ± 0.020 (95% ci) µmol C L^{-1} d^{-1}, with again no significant differences in slope found between the two size fractions. Ciliate growth and grazing was thus estimated at 11% C d^{-1} and 37% C d^{-1}, respectively. When applied to the biomass distributions at the other stations, integrated ciliate grazing was cautiously estimated to be 2–34 mmol C m^{-2} d^{-1}, potentially accounting for 1–20% of NPP (Table 7).

Mesozooplankton grazers ingested 1.3–11 mmol C m^{-2} d^{-1} in the upper 100 m of the water column, or 1–3% of NPP (Table 7). These low grazing rates suggest that mesozooplankton have little impact on removal of the phytoplankton bloom from surface waters within the polynya during the time of sampling. When added to the microzooplankton grazing rates estimated above, 17–67% of NPP (average = 34 ± 16%, n = 8) could be consumed by grazers in the upper water column. Between 100 and 350 m, mesozooplankton grazing ranged from 1.6 to 9.2 mmol C m^{-2} d^{-1} and accounted for an additional 1–4% of NPP. At the four deeper trough stations (13, 50, 57, and 68), the grazing estimated below 350 m (Table 7) contributed 32–58% (4.7–17 mmol C m^{-2} d^{-1}) of the total water column mesozooplankton grazing (4.2–25 mmol C m^{-2} d^{-1}). Summing the available grazing rates (we do not have any estimates of microzooplankton grazing below 100 m), we calculated the total potential grazing contribution to be 53-110 mmol C m^{-2} d^{-1}, or 22–46% of NPP (Table 7).

Table 7. Integrated biological productivity over the upper water column and grazing rates in upper and subsurface waters

Station grouping[a]	Station #[b]	Upper water column rates[c] (0–100 m, mmol C m^{-2} d^{-1})											Subsurface water, mesozoop grazing				All depths, total mesozoop grazing[b]	All grazers, all depths (0–>350 m)	
		NPP	BP	BP / NPP (%)	CIL grazing[d]	CIL grazing / NPP (%)	DINO grazing[d]	DINO grazing / NPP (%)	Mesozoop grazing		All grazing[e]	All grazing/ NPP (%)	100–350 m		> 350 m			Total grazing	Grazing / NPP (%)
									Night	Day			Night	Day	Night	Day			
Early bloom	5	84	1.8	2.1	-	-	-	-	-	-	-	-	-		-	-	-	-	-
	68	165	4.4	2.7	17	10	30	18	5.1	3.8	51	31	5.9	3.8	9.4	4.7	16	63	38
	6	325	11	3.2	-	-	-	-	-	-	-	-	-	-	-	-	-	-	-
	34	333	12	3.5	11	3	44	13	-	-	54[f]	16	-	-	-	-	-	-	-
	66	206	11	5.5	18	9	53	26	-	-	71[f]	34	-	-	-	-	-	-	-
Mid-bloom	18	244	10	4.2	-	-	-	-	-	-	-	-	-	-	-	-	-	-	-
	13	270	14	5.4	2	1	35	13	11	7.0	46	17	4.1	6.8	8.7	4.9	21	58	22
	25	182	10	5.7	9	5	40	22	3.7	1.5	52	28	1.6	1.6	-	-	4.2	53	29
High bloom	50	237	13	5.7	16	7	77	33	4.9	3.9	97	41	7.7	3.3	6.8	7.1	17	110	46
	35	294	18	6.0	-	-	-	-	2.4	1.3	-	-	4.4	8.1	-	-	8.1	-	-
	48	168	16	9.4	34	20	78	47	-	-	112[f]	67	-	-	-	-	-	-	-
	29	256	13	5.0	-	-	-	-	-	-	-	-	-	-	-	-	-	-	-
	57	196	11	5.6	25	13	38	20	1.7	2.9	65	33	9.2	7.3	17	12	25	88	45

[a]By bloom stage, as shown in Figure 4
[b]Arranged in order of increasing nitrogen drawdown (ΔDIN)
[c]NPP = net primary production, BP = bacterial production, CIL = ciliates, DINO = dinoflagellates
[d]Approximate only; estimated by applying grazing rates from Sta. 35 (12 m) to biomass distribution at other stations
[e]Using average of day and night rates for mesozooplankton
[f]May be underestimate; includes only microzooplankton rates
doi: 10.12952/journal.elementa.000140.t007

NCP and export calculations

Estimates of gas exchange indicated that some CO_2 (up to 1.71 mol C m^{-2}; Table 8; Figure 11) could have been added to the surface DIC inventory from the atmosphere, contributing up to 29% of *s*NCP, primarily at the high bloom stations. The *s*NCP ranged from 0.22 to 5.89 mol C m^{-2} (Table 8). At the two high bloom stations with the highest *s*NCP, Stations 35 and 57, nearly half of *s*NCP was observed as ΔPOC still present in the upper water column (Figure 11). Much smaller and variable fractions were found in ΔDOC and ΔZOOP (Figure 11; Table 8).

Table 8. Summary of carbon inventories, quantities, and export calculations[a]

Station grouping[b]	Station #[c]	Changes in carbon inventories and quantities (mol C m^{-2})						Exported C quantity (mol C m^{-2})	Exported C flux (mmol C m^{-2} d^{-1})	Trap C flux (mmol C m^{-2} d^{-1})			
		ΔDIC	GasEx	*s*NCP	ΔPOC	ΔDOC	ΔZoop	sExportC	Export C	Drifting			Moored
										60 m	150 m	300 m	365 m
Early bloom	5	0.21	0.00	0.22	0.18	(–0.04)	0.032[e]	0.04	1.7	-[f]	-	-	-
	68	0.95[d]	0.00	0.95	0.71	(–0.14)	0.036	0.35	44	-	-	-	-
	6	1.35[d]	0.03	1.38	1.56	0.75	0.032[e]	(–0.96)	(–64)	-	-	-	-
	34	1.56[d]	0.00	1.56	1.98	(–0.09)	0.032[e]	(–0.37)	(–31)	-	-	-	-
	66	1.57	0.00	1.57	1.54	0.40	0.032[e]	(–0.40)	(–29)	-	-	-	-
	AVE	1.13	0.01	1.14	1.19	0.18	0.03	0.20	22.9				
	S.D.	0.57	0.01	0.57	0.73	0.39	0.00	0.22	29.9				
Mid-bloom	18	2.05[d]	0.00	2.05	2.03	0.89	0.032[e]	(–0.91)	(–38)	-	-	-	-
	13	1.92	0.79	2.71	1.87	0.26	0.169	0.40	7.1	-	-	-	-
	25	2.92	0.57	3.49	1.98	1.13	0.023	0.35	9.3	-	-	-	-
	AVE	2.30	0.45	2.75	1.96	0.76	0.07	0.38	8.20				
	S.D.	0.54	0.41	0.72	0.08	0.45	0.08	0.04	1.56				
High bloom	50	3.74	1.33	5.06	2.23	1.21	0.066	1.55	36	-	-	-	-
	35	4.18	1.71	5.89	2.80	1.39	0.027	1.68	35	18	3.0	0.98	-
	48	3.99[d]	1.62	5.62	3.23	(–1.11)	0.032[e]	3.47	75	-	-	-	-
	29	4.26[d]	1.00	5.26	2.77	(–0.18)	0.032[e]	2.64	64	-	-	-	-
	57	4.71	0.58	5.29	2.29	(–0.21)	0.016	3.20	53	27	2.7	2.2	3[g] (8)[h]
	AVE	4.18	1.25	5.42	2.66	0.22	0.03	2.5	52.6				
	S.D.	0.36	0.47	0.33	0.41	1.06	0.02	0.9	17.4				

[a]Integrated carbon inventories and quantities (to T_{min_100}) used to infer export, with comparisons to other ASP export estimates
[b]By bloom stage, as shown in Figure 4
[c]Includes averages for station groupings, with standard deviations (S.D.)
[d]Stations where ΔDIC data were filled in using ΔDIN and ΔDIC:ΔDIN = 6.6
[e]Stations where ΔZoop was filled in using median of six measured stations
[f]Indicates not available. The C flux for drifting traps was calculated from P flux and the station's ΔPOC:ΔPP ratio (Table 4).
[g]Flux at the same time of Sta. 57 sampling; relative trap efficiencies of drifting versus moored designs not known
[h]Peak flux in mid-January after ASPIRE departed
doi: 10.12952/journal.elementa.000140.t008

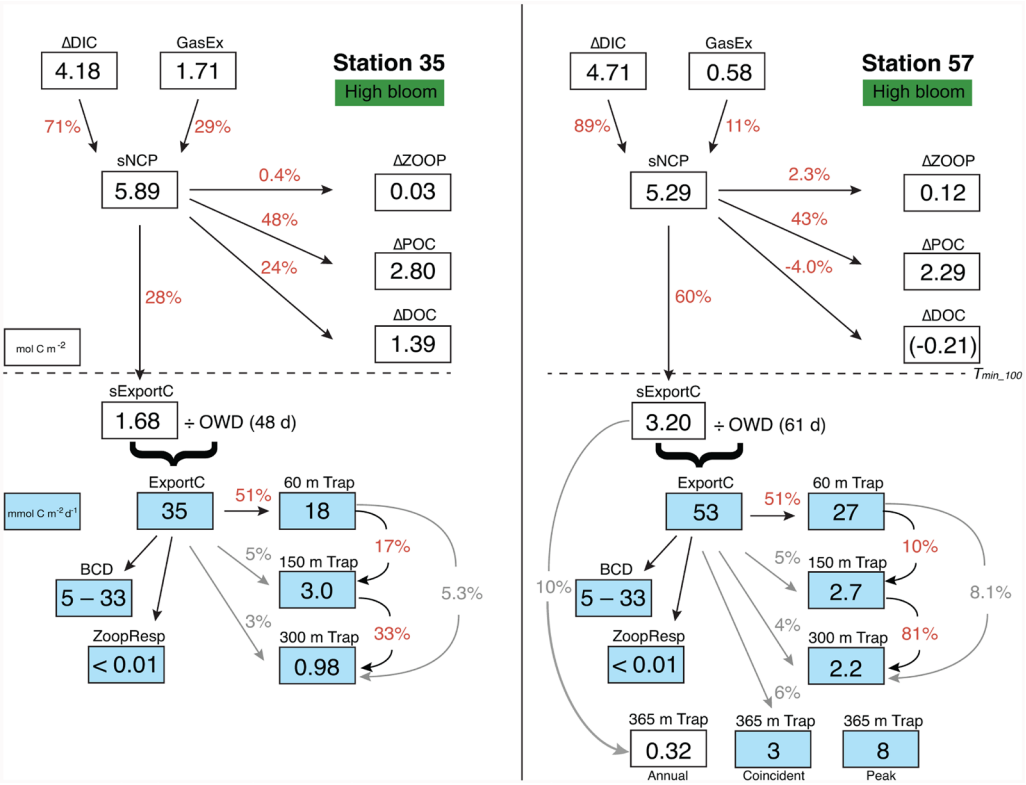

Figure 11

Carbon budgets for two peak bloom stations in the ASP.

Values for carbon budget inventories (white boxes, mol C m^{-2}) and fluxes (blue boxes, mmol C m^{-2} d^{-1}) measured directly at two high bloom stations (35 and 57), with percent transfers in red. Seasonal net community production (*s*NCP) is the sum of the integrated observed drawdown in dissolved inorganic carbon (ΔDIC) and gas exchange (GasEx). Some of the *s*NCP contributes to the buildup of mesozooplankton biomass (ΔZoop), particulate organic carbon (ΔPOC), and dissolved inorganic carbon (ΔDOC). The remainder is seasonal export (*s*ExportC). This inventory is converted to a rate (ExportC, in blue) by dividing by the number of open water days (OWD). The export rate can then be compared to flux measurements from drifting traps at 60 m, 150 m, and 300 m depths, and the moored trap at 365 m. Drifting traps and the moored trap capture efficiencies were not intercalibrated, so comparisons are qualitative only. The two rate values for the 365 m trap are for the time at station (coincident, left) and at the peak flux (about ten days later, right). The remaining Export C flux is mostly accounted for with bacterial carbon demand (BCD) and zooplankton respiration (ZoopResp); see Ducklow et al. (2015). The total annual export (0.32 mmol C m^{-2}) to the moored trap (365 m) is ~10% of the seasonal *s*ExportC inventory (3.2 mmol C m^{-2}) at the time of the ASPIRE sampling Sta. 57 on December 31.

doi: 10.12952/journal.elementa.000140.f011

After subtracting organic inventories from *s*NCP, *s*ExportC estimates ranged from –0.96 to 3.47 mol C m^{-2}, with five stations (mostly early bloom: 68, 6, 34, 66, and 18) indicating net carbon import, and eight stations (mostly high bloom: 5, 13, 25, 50, 35, 48, 29, and 57) showing positive carbon export. The stations exhibiting positive export tended to have longer OWD and greater nutrient drawdown (ΔDIN). Sta. 35 notably had a large ΔpCO_2 deficit and rapid gas exchange, with about equal contributions to ΔDOC and export (Figure 11). In contrast, Sta. 57 was more deeply mixed, had a smaller ΔpCO_2 deficit, less gas exchange (at the time of observation), but no observed buildup of ΔDOC; consequently, *s*ExportC at Sta. 57 was greater than at Sta. 35.

Where *s*ExportC was positive (Stations 5, 13, 25, 50, 35, 48, 29, 57), the inferred Exported Fraction (Export C / *s*NCP) accounted for 10–62% of the total potential export estimated by the available *s*NCP (Table 9). Because of the tight correlation between ΔDIC and ΔDIN, the *s*NCP, *s*ExportC, and Exported Fraction all correlated significantly (Table 9) with ΔDIN ($R > 0.66$, $n = 13$, $p < 0.01$) and OWD ($R > 0.53$, $n = 13$, $p < 0.05$).

When dividing the *s*ExportC by a relevant time scale (OWD; Table 1), the Export C flux ranged from –64 (import) to 75 mmol C m^{-2} d^{-1} (export; Table 8). For the two stations where we have drifting sediment trap deployments (Stations 35 and 57; Table 8; Figure 11), the inferred export fluxes were somewhat larger than, but within a factor of two of, the trap fluxes directly measured at 60 m (18–27 mmol C m^{-2} d^{-1}; Table 8; Figure 11), a reasonable match given that the capture efficiency of the drifting traps is not known. The comparison between Export C and the moored trap fluxes from the same or later time intervals, revealed sharp declines (only 6% of ExportC getting to 365 m at the time of sampling; Figure 11) in sinking material from the base of the surface layer to 365 m (Table 8; Figure 11), suggesting rapid remineralization in the mid-depths (see Ducklow et al., 2015; Williams et al., 2016).

When *s*NCP was converted to a rate (NCP; using OWD) and compared to NPP (Table 9), the export efficiency (NCP/NPP) ranged from 10 to 73% (average for high bloom stations = 52 ± 12%, $n = 5$). Once converted to a rate, the correlations of NCP or export efficiency with ΔDIN were no longer significant ($R < 0.43$, $n = 13$, $p > 0.05$; Table 9).

If we did not assume a bloom time scale, and instead calculated a turnover time (the ratio of *s*NCP:NPP), values ranged from 2.6 to 32 days with an average for high bloom stations of 24 ± 5 days. This estimate of the turnover time correlated significantly ($p < 0.01$) with ΔDIN and OWD (Table 9), further corroborating the bloom gradient as a useful construct in this system.

As expected (by definition), changes in seasonal inventories (such as *s*NCP and sExportC) tended to increase with ΔDIN through the early, mid-, and high bloom stages. We note, however, that once scaled by time, many of the rates (e.g., NCP and NPP) were steady through all three bloom stages (Table 9). Similarly, exported fraction and particle export efficiency (ExportC/NPP) increased with bloom stage, but export efficiency (NCP/NPP) did not (Table 9).

Table 9. Comparison of net primary production (NPP), net community production (NCP), and inferred export quantities and rates

Station grouping[a]	Station #[b]	NPP (mmol C m^{-2} d^{-1})	NCP and Export						
			Seasonal quantities			Rates		Particle export efficiency (ExportC rate / NPP, %)	Turnover time ($_s$NCP / NPP, days)
			$_s$NCP (mol C m^{-2})	sExportC (mol C m^{-2})	Exported fraction (%)	NCP (mmol C m^{-2} d^{-1})	Export efficiency (NCP/NPP, %)		
Early bloom	5	84	0.22	0.04	20	8.4	10	2.0	2.6
	68	165	0.95	–0.32	(–33)	119	72	-	5.8
	6	325	1.38	–0.96	(–69)	92	28	-	4.3
	34	333	1.56	–0.37	(–24)	130	39	-	4.7
	66	206	1.57	–0.40	(–26)	112	54	-	7.6
	AVE	223	1.14	–0.40	-[c]	92	41	-	5.0
	S.D.	107	0.57	0.36	-	49	24	-	1.9
Mid-bloom	18	244	2.05	–0.91	(–44)	85	36	-	8.5
	13	270	2.71	0.40	15	48	18	2.6	10
	25	182	3.49	0.36	10	92	51	5.1	19
	AVE	229	2.75	–0.05	13	75	35	4	13
	S.D.	44	0.72	0.75	4	24	17	2	5.7
High bloom	50	237	5.06	1.55	31	119	50	15	21
	35	294	5.89	1.68	28	123	42	12	20
	48	168	5.62	3.47	62	122	73	45	32
	29	256	5.26	2.64	50	128	50	25	21
	57	195	5.29	3.20	60	87	45	27	27
	AVE	230	5.42	2.51	46	116	52	25	24
	S.D.	50	0.33	0.87	16	16	12	13	5
All stations	$R_{\Delta DIN}$[b]	–0.15	**0.96**	**0.86**	**0.75**	0.43	0.37	**0.68**	**0.92**
	R_{OWD}[b]	–0.05	**0.79**	**0.73**	0.64*	–0.13	–0.08	0.32	**0.76**

[a]By bloom stage, as shown in Figure 4
[b]Includes averages for station groupings, with standard deviations (S.D.), and polynya-wide correlation (R) of each variable with ΔDIN and with open water duration (OWD) (significant correlations: $p < 0.01$ in bold, $p < 0.05$ with asterisk)
[c]Indicates not available
doi:10.12952/journal.elementa.000140.t009

Discussion

An extremely strong and efficient biological pump

The ASPIRE observations support the designation of the ASP as one of the most productive bloom systems in the world. Both the strength and efficiency of the biological pump (*sensu* Sarmiento et al., 2004) are high relative to other ocean systems. Clearly, the capacity for nitrate and carbon drawdown in the ASP is large, once this area is released from micronutrient and light limitation (Alderkamp et al., 2015; Sherrell et al., 2015; Schofield et al., 2015). The early season surface nitrate concentration (~31 μmol L^{-1}) is near the global maximum (World Ocean Atlas, 2001) and nitrate concentration in upwelling mCDW is even higher (33.5 μmol L^{-1}; Table 2). With the iron supplied in association with the melting ice sheet (Yager et al., 2012; Sherrell et al., 2015), nitrate at the surface was reduced to as low as 7.2 μmol L^{-1} during our late December observations, giving a biological pump efficiency (based on surface nitrate depletion relative to subsurface nitrate concentration) of ~80%, similar to the North Atlantic and North Pacific (Sarmiento et al., 2004). Unlike those other ocean areas, however, the exported carbon flux (the strength of the pump) was also very high (up to 75 mmol C m^{-2} d^{-1}). Coastal polynyas often have shallow mixed layers created by melting seasonal sea ice and enhanced by solar heating that provide a favorable physical environment for phytoplankton growth as long as nutrients are available (Smith and Barber, 2007). Relatively shallow mixed layers (average = 25 ± 19 m) in the ASP relieved the light limitation common in most other parts of the Southern Ocean, although self-shading may have become an issue during the high bloom stage (Schofield et al., 2015).

Net Primary Production

Maximum NPP observed (up to 333 mmol C m^{-2} d^{-1}, or 4 g C m^{-2} d^{-1}) exceeded reports from most other coastal polar ecosystems (Northeast Water: 1.1 g C m^{-2} d^{-1}, Smith, 1995; Barents Sea: 1.1 g C m^{-2} d^{-1}, Luchetta et al., 2000; Chukchi Shelf: 2.4 g C m^{-2} d^{-1}, Chen et al., 2002; Cape Bathurst Polynya: 2.7 g C m^{-2} d^{-1}, Arrigo and van Dijken, 2004; West Greenland Sea: 3.2 g C m^{-2} d^{-1}, Jensen et al., 1999) except the North Water polynya (~6 g C m^{-2} d^{-1}; Mei et al., 2003) which receives a steady supply of limiting nitrate from the southward flowing Polar Surface Water (Tremblay and Smith, 2007) and the Fram Strait during peak rates in a springtime *Phaeocystis* bloom (~8 g C m^{-2} d^{-1}; Smith et al., 1991).

Mesozooplankton community ingestion rates and grazing impact are within a range similar to those published for other Southern Ocean systems (Lee et al., 2013; Bernard et al., 2012; Pakhomov and Froneman, 2004; Atkinson et al., 1996). Zooplankton grazing cleared < 2.5% of primary production in South Georgia Island, Antarctica (Atkinson et al., 1996). Lee et al. (2013) also reported generally low grazing impact of mesozooplankton within the Amundsen Sea Polynya (< 1%) and no correlation between Chl *a* and zooplankton ingestion rates.

Our relatively low zooplankton biomass results were similar to those of the nearby Ross Sea (Huntley and Zhou, 2000; Tagliabue and Arrigo, 2003), where primary productivity is also high. A somewhat higher zooplankton biomass was observed in Terra Nova Bay, hypothesized to be better able to keep up with the slower growing diatom population there (Tagliabue and Arrigo, 2003). Zooplankton biomass is an order of magnitude higher in the vicinity of South Georgia Island (Ward et al., 1995) and at the Antarctic Polar Front (Fransz and Gonzalez, 1997). In the Northeast Water Polynya (Arctic), results similar to ours were observed, with lower zooplankton abundances inside vs. outside the open water area (Ashjian et al., 1997). Zooplankton are not necessarily significant consumers of the primary production within polynyas during a spring bloom (less than 10% in the Arctic's North Water polynya; Saunders et al., 2003) due to high primary production rates and low abundance of zooplankton (Ashjian et al., 1997; Deibel and Daly, 2007). There is little evidence that polynyas are food limited (Deibel and Daly, 2007); late summer may be a more important time for higher trophic levels.

Calanoides acutus dominated the mesozooplankton community within the ASP (Wilson et al., 2015). *C. acutus* has been shown to select heterotrophic microplankton over phytoplankton (Calbert et al., 2006) and may be feeding selectively within the ASP rather than using the dominant phytoplankton species (*P. antarctica*), which is known to produce potentially toxic acrylic acid (Sieburth, 1959, 1960, 1961). Wilson et al. (2015) show a negative correlation between zooplankton abundance and the proportion of *Phaeocystis* in the phytoplankton.

Although the fate of NPP within the upper mixed layer seemed uncoupled from mesozooplankton populations, it showed some connection with heterotrophic microzooplankton and bacteria. Grazing by ciliates and dinoflagellates in the upper water column could have consumed for a significant fraction (14 –67%) of NPP. Still, the estimated dinoflagellate and ciliate grazing rates were at the lower end of what has been reported in other studies from the Southern Ocean (4 ± 2% d^{-1} of Algal C, 34 ± 16% d^{-1} of NPP_{100}; Froneman and Perissinoto, 1996; Froneman and Balarin, 1998; Froneman, 2004). Furthermore, large colonial *Phaeocystis* are not easily grazed by microzooplankton (Caron et al., 2000; Nejstgaard et al., 2007), thereby reducing the amount of fixed carbon that could be recycled in the upper mixed layer within the microbial loop via the protozoans (Froneman and Perissinoto, 1996). Although *P. antarctica* was the dominant phytoplankton group, there were other primary producers such as sea ice algae and diatoms to support higher trophic levels (Table 6). Indeed, during the early bloom, the "negative" export could be explained by net import of ice algal carbon that could fuel some bacteria (Sipler and Connelly, 2015) or zooplankton (ice krill found at Sta. 66; Wilson et al., 2015).

For the stations where we have estimates for both grazing size classes, however, exported carbon flux (Table 8) correlated positively (r = 0.85, n = 6) with the "All grazing (0–100 m)" fraction of NPP (Table 7), so it seems that additional grazing does not reduce export.

Bacterial production accounted for only a small fraction of the fate of NPP, but growth efficiencies were quite low and the integrated bacterial carbon demand in the upper 100 m (0.8–2.8 g C m^{-2} d^{-1}) could have consumed a large fraction (25–128%, median = 43%) of NPP during ASPIRE's bloom development (Williams et al., 2016). As some bacteria may be in mutualistic associations with the *Phaeocystis* (Delmont et al., 2014, 2015), further investigation of these microbial linkages is warranted.

Net Community Production

Despite these heterotrophic demands on NPP, the magnitude of NCP in the ASP was still greater than that of most other well-studied polynyas around the world (Northeast Water: Yager et al., 1995; Weddell Sea: Hoppema et al., 1999; Brown et al., 2015; Ross Sea: DiTullio et al., 2000; North Water, Miller et al., 2002; Miller and DiTullio, 2007) and about a factor of two larger than NCP values reported from the Palmer-LTER region west of the Antarctic Peninsula (2–54 mmol C m^{-2} d^{-1}; Huang et al., 2012), which is located at a lower latitude range (64–70°S) than the ASPIRE area. The ASP exhibited higher surface and integrated

Chl *a* concentrations, and ΔDIC than the extensive, early season (18 December–08 January) *Phaeocystis* bloom observed by the ROAVERRS project in the more southern Ross Sea Polynya (RSP; Arrigo et al., 1999; DiTullio et al., 2000) and greater ΔPOC and ΔDIN than the spring *Phaeocystis* bloom in the Greenland Sea (Smith et al., 1991). Although estimated differently, NCP in ASP was more comparable to the values reported for the highly productive North Water (April–July average = 93 mmol C m^{-2} d^{-1}; Tremblay et al., 2002) and to rates reported for summertime conditions in the much shallower Chukchi Sea (Bates et al., 2005), with both of those Arctic ecosystems dominated by diatoms.

With ASPIRE sampling during the buildup stages of the bloom, the estimated NCP in the ASP (up to 130 mmol C m^{-2} d^{-1}) was comparable to the intense spring bloom observed in the North Atlantic during a week in May (115 mmol C m^{-2} d^{-1}; Alkire et al., 2012). Because ASPIRE departed from the region before the productivity peak observed by satellite, the annual NCP is very likely greater than we measured as *s*NCP. If the observed *s*NCP in the ASP (up to 5.9 mol C m^{-2} on 31 December) represented the region's entire production for the year (i.e., in the unlikely event that the bloom shut down the day ASPIRE departed), it would still exceed the annual NCP for most non-polar regions (2–4 ± 1 mol C m^{-2} $year^{-1}$; Emerson, 2014). Notably, the late December maximum *s*NCP measured during ASPIRE is already 67% of the mean total annual production (for 1998–2014) estimated by satellite (8.8 ± 1.8 mol C m^{-2}; Arrigo et al., 2015).

The seasonal net community production measured in the ASP during December was most comparable to the late season RSP where *s*NCP values ranged from 1.2 to 11 mol C m^{-2} during mid-January to early February across three distinct eco-regions, with a regional average of 4.8 ± 1.9 mol C m^{-2} (Sweeney et al., 2000), similar to the late December value of 5.9 mol C m^{-2} at ASP Sta. 57. Values for *s*NCP during ASPIRE were most similar to the northern edges of the RSP (Region III; 1.2–4.2 mol C m^{-2}; at latitudes similar to ASP), which also had shallow mixed layer depths (average = 27 m; similar to ASP), remnant WW, and intrusion of mCDW from depth. This region of the RSP was thought to have lower NCP compared to the more productive regions to the south because of either light or micronutrient limitation. The ASP, though, presumably had the potential to continue to bloom during the remaining summer months.

Most stations in the ASP differed from Region III of the RSP, however, in having a much lower ΔSi:*s*NCP_{max} ratio (median = 0.08, versus 0.10–0.31 in the RSP; Sweeney et al., 2000), and by being dominated (more than 80% at most stations; Table 6) by *P. antarctica* rather than by diatoms. Only four stations in the ASP (68, 13, 29, and 57) exhibited ΔSi:NCP ratios ≥ 0.10, reflecting some diatom influence over the course of the bloom, and only two stations (68 and 6; Table 6) showed diatoms contributing significantly to the phytoplankton assemblage at the time we sampled. Because *Phaeocystis* can enhance carbon drawdown relative to diatoms (Arrigo et al., 1999), this difference in phytoplankton assemblage likely influences the biogeochemical cycling and relative carbon flux of the two areas. Stoichiometric ratios for changes in inorganic and organic inventories in the ASP fell between those for diatom- and *Phaeocystis*-dominated waters in the RSP (Arrigo et al., 1999), but tended more toward the latter.

High bloom stations in the ASP (e.g., 50, 35, 48, 29 and 57), with *s*NCP values > 5 mol C m^{-2}, resembled observations reported from the *Phaeocystis*-dominated central region of the RSP (Region II; Sweeney et al., 2000), where *s*NCP ranged from 4.4 to 11 mol m^{-2} and ΔSi:*s*NCP was 0.04 ± 0.02. This favorable comparison suggests that if ASPIRE had sampled later into the summer, we would have likely confirmed *s*NCP even higher than in the central RSP (on a per meter squared basis, as suggested by satellite observations; Arrigo and van Dijken, 2003; Arrigo et al., 2012, 2015), although the causes for the ASP bloom termination (well prior to return of the sea ice; Arrigo and van Dijken, 2003) are unknown, and its timing is variable.

An export-dominated ecosystem?

The inferred export from the upper water column of the polynya during the ASP bloom (up to 75 mmol C m^{-2} d^{-1}) was larger than we expected for a developing bloom, particularly relative to other well-studied marine environments (Berelson, 2001). It was greater by far than the estimated fecal pellet production (3.2–9.3 mmol C m^{-2} d^{-1}; Ducklow et al., 2015), but agreed reasonably well (within a factor of two when available; Figure 11, Table 8) with direct measures of export from the shallow drifting sediment traps that captured mostly sinking phytodetritus. Although *Phaeocystis* phytodetritus is generally considered to be a low-efficiency vector for particle flux (Beaulieu, 2002; Reigstad and Wassmann, 2007; Turner, 2015), exceptions have been observed in both northern and southern polar ecosystems (Wassman et al., 1990; Smith et al., 1991; DiTullio et al., 2000; Bauerfeind et al., 2009; Le Moigne et al., 2015). Ducklow et al. (2015) reported *Phaeocycstis* aggregates in the ASP moored trap at Sta. 57.

Particle export efficiency (*e* = ExportC rate/ NPP) was low during the early and mid-bloom periods, suggesting that the near-surface polynya retained carbon (Wassmann, 1998) during the early season. It increased, however, during the high bloom, with three of the stations exceeding 0.2, but only one station exceeding *e* > 0.4. An alternate measure of export efficiency (NCP / NPP) gave higher values during the high bloom, but was also high during the other stages. These efficiencies were high relative to other marine systems (Berelson, 2001) including some in polar latitudes (Sweeney et al., 2000), although this outcome may be because we used ^{14}C-bicarbonate uptake incubations to assess NPP instead of using the preferred oxygen isotope method for GPP (Quay et al., 2010).

Such rate-based calculations depend on matching up appropriate time scales, however, and are likely sensitive to the point in time when ASPIRE sampled. When seasonal quantities were compared instead, the estimate for the exported fraction (sExportC / $_s$NCP) was high for the high bloom stations only. These export fractions (average = 46 ± 16%) were comparable to those observed in the RSP much later in the summer (Sweeney et al., 2000), but do not reach the extremely high fractions of the extraordinary ROAVERRS bloom observations during the early season RSP (~80%; DiTullio et al., 2000).

If ~50% of the annual ASP production of 8.8 ± 1.8 mol C m^{-2} (from satellites; Arrigo et al., 2015) were exported, that would generate an export of 4.4 mol C m^{-2} over an average area of 31,844 ± 4679 km^2, or 0.14 ± 0.02 Tmol C per year (1.7 ± 0.25 Tg C y^{-1}). This ASP export estimate is similar to the estimate for CO_2 uptake by the central polynya during the early season (1.3 ± 0.6 Tg C; Mu et al., 2014). The ASP contributes 2–3% of the Southern Ocean CO_2 uptake in about 0.25% of the area, a approximate 10-fold enhancement, suggesting that something special is going on in the ASP.

A few of the stations (6, 34, 66, and 18) exhibited negative export (or import). Interestingly, all of these stations still had some sea ice present. Thus, in addition to its contributions of fresh water to the water column (up to 2%), the sea ice may be contributing more organic matter (either as DOC or POC) than we expected. Although we tried to account for these contributions in our mixing model, sea ice communities are extremely patchy and variable (Thomas and Dieckmann, 2010; Fransson et al., 2011). Heterogeneous contributions from the melt could explain how more organic matter was observed than could be explained by changes in inorganic carbon inventories alone. Gas exchange through partial sea ice cover could also explain the mismatch for we assumed that exchange to be negligible. Microbial utilization of DOC from sea ice is rapid (Sipler and Connelly, 2015), but incorporation to biomass may not be particularly efficient (Williams et al., 2016), so we would not likely see these inputs linger, as they would be respired back to DIC. Subsurface contributions of organic matter, imported from the sediments or deep water, also need to be constrained better to improve confidence in these export estimates. Concentrations of DOC in WW and mCDW (69 and 76 µmol C L^{-1}; Table 2) were higher than expected for deeper water in the Southern Ocean (usually about 45 µmol L^{-1}; Hansell et al., 2009), perhaps reflecting benthic inputs. Given their higher nutrient and DOM concentrations, upwelling or mixing of deep waters into the euphotic zone would enhance nutrient availability and also influence the estimates of NCP and export. Horizontal advection could also explain some of the imbalance, but is not required given the known inputs from the sea ice and sea floor.

Subsurface remineralization

Once settled into the subsurface, however, the exported material was susceptible to microbial degradation. Estimated rates of bacterial respiration in the mesopelagic were sufficient to account for the difference between the ExportC flux from the surface layer and the material captured in the moored sediment trap (Ducklow et al., 2015; Williams et al., 2016). If the *Phaeocystis* colonies break up into single cells (perhaps by turbulence) once they sink into the mid-waters, they would become more susceptible to microzooplankton grazing and bacterial degradation (Wassmann, 1993). Microbial degradation of the sinking flux in the ASP may be more determined by particle-associated microbial activity (Delmont et al., 2014; Williams et al., 2016) than in other marine systems, although subsurface microbial breakdown of POC is probably more complex and widespread than previously thought (Kellogg et al., 2011; Collins et al., 2015). The fraction of exported particulate carbon that sank to greater depths (>150 m) ranged from 3 to 6% at the time of sampling, and was low compared to most other ocean ecosystems (Buesseler and Boyd, 2009). A similar decline in the deep flux was seen in the Ross Sea (Collier et al., 2000), however, and in two Arctic polynyas (Tremblay et al., 2012), presenting the possibility that low export efficiency to greater depths may be typical of biologically productive polar seas, whether Antarctic or Arctic.

Applying the Martin equation to the drifting trap profile for the decline in particle flux with depth ($POC\ flux_z = POC\ flux_{100}\ (z / 100)^b$, where z is depth below 100 m and b is a fitting parameter that increases with decay rate; Martin et al., 1987), gives b values for both deployments of ~1.8, greater than those found in other marine environments (where b ranges from 0.6 to 1.3; Berelson, 2001). Using instead our estimated ExportC from the upper water column and assuming the deep traps were perfectly efficient gives an even higher b (> 3) for both stations where we have trap data. A high b value was not entirely unexpected, given the very high productivity and export quantities from the upper water column, but the ASP b values were even higher than the linear relationship from other studies would predict (e.g., Fig. 6 in Berelson, 2001), suggesting non-linearity in extremely high productivity regions or regions dominated by *Phaeocystis*. The timing of ASPIRE may also be playing a role. The behavior of the sinking POC we observed in the ASP during the early season may be unique in the absence of significant grazing pressure from mesozooplankton. Model simulations that could be used to estimate advective fluxes in this region would also improve our understanding of spatial heterogeneity and the long-term fate of the carbon, especially given that the ultimate destination of these midwaters and their time scale for potential outgassing is poorly known.

A key question relates to what happened in the region after ASPIRE departed. The carbon flux into the moored sediment trap more than doubled between the sampling of Sta. 57 in late December and the peak trap flux in mid-January (Ducklow et al., 2015). This increase suggests an increase in productivity, an increase

in the exported fraction, or a lag in the sinking of the export from December. Certainly there was adequate ΔPOC available in the upper water column to support the increased flux later in January (see Figure 11; total annual capture in the moored trap was 0.3 mol C m^{-2}; Ducklow et al., 2015). The mechanisms triggering the *Phaeocystis* to sink in the late season ASP are unknown, but likely involve a regionally specific combination of physics and ecology (Wassmann, 1993). The same passing icebergs, eddies, or winds that trigger deep mixing and enhance nutrient flux to the surface, extending the bloom, would also facilitate the downward flux of surface particles. In support of this idea, the exported fraction (60%) at iceberg-impacted Sta. 57, which also had the longest OWD and the deepest mixed layer, was notably one of the highest in the region. A late season export event in the Ross Sea was driven by pteropods (Collier et al., 2000) following a diatom bloom triggered by a wind event. In the ASP, zooplankton fecal pellets contributed increasingly to material collected by the moored trap during the summertime peak flux, but they were dominated by those produced by mid-sized copepods such as *Metridia gerlachei* (Ducklow et al., 2015).

Three-dimensional ocean dynamics and links to the melting ice sheet

In the ASP, macronutrients are initially replete, allowing for large accumulations of biomass and high net community production (Eppley, 1989), as long as there is an adequate supply of trace nutrients like iron. Iron often controls the primary productivity in areas where macronutrients are abundant (Sunda and Huntsman, 1998; Moore et al., 2013), and incubation studies suggest that the rate of bloom development in the ASP is controlled by delivery rate of Fe to the euphotic zone (Alderkamp et al., 2015). Several sources of iron may contribute to the exceptional productivity of the ASP (Yager et al., 2012; Sherrell et al., 2015) and the supply of iron to this ecosystem is intimately linked to the melting ice sheet and the physical delivery of iron- and meltwater-rich deep water to the euphotic zone (see Randall-Goodwin et al., 2015; Sherrell et al., 2015). This important discovery from ASPIRE implies a three-dimensional pathway for iron, from the Dotson Ice Shelf cavity to the euphotic zone of the ASP bloom region located 20–100 km offshore. Such a 3-D pathway differs from the traditional one-dimensional view, where nutrients are injected into the euphotic zone by vertical mixing. More complex physical mechanisms, where mesoscale structures and eddies may play a central role, may need to be invoked to account for the transport of Fe from the ice shelves to the ASP. Modeling studies are currently ongoing to investigate controls on the iron flux to the central ASP and the sensitivity of this flux to future increases in ice-sheet melting. Whether increasing rates of ice-sheet melt (Mouginot et al., 2014; Joughin et al., 2014) will lead to more iron delivery and more productivity in the ASP remains to be determined.

This iron delivery process, which likely varies regionally, also imposes a multi-dimensional framework on what would otherwise be a fairly straightforward one-dimensional calculation of NCP. We have assumed in our calculations that the wintertime water column is well-mixed and has the same properties throughout the upper 100 m. The same processes that deliver iron to the surface also modify the "wintertime" conditions against which we measured observed inventories, impact our ability to estimate changes from these variable endmember values, and potentially set the initial conditions constraining the subsequent bloom. In the absence of direct wintertime observations, these heterogeneities increase the uncertainties in the calculations and highlight the need to move away from traditional one-dimensional balances to explain biogeochemical processes in this system.

Because of seasonal inaccessibility and the difficult ice environment for moorings that measure near-surface variables over time, we lack knowledge about whether the WW truly resets to the same physical and biogeochemical conditions across the region, confounding the simple mixing model approach and requiring the use of "local" endmembers for each station that estimate the most recent winter conditions at each location. We estimated the WW conditions just prior to the 2010–11 spring melt from the conditions at the lowest temperature observed in the upper 100 m. This approach does not require conditions to be reset to the same values every year. In fact, some of the unexplained interannual variability reported for this region (Arrigo and van Dijken, 2003; Arrigo et al., 2012, 2015) could be related to variable subsurface conditions at the initiation of the bloom season, driven in part by variable meltwater inputs from the ice sheet. Ultimately, we need better dynamic understanding of wintertime conditions and ocean mixing processes in the region, along with better tracers of the different water mass contributions to the upper water column of the ASP.

Because of large spatial heterogeneity and the observed 3-D nature of ocean circulation and micronutrient delivery in this area, greater confidence in a more refined regional carbon budget will require high-resolution ocean and biogeochemical numerical modeling. These efforts are currently underway and will no doubt guide improved observations of this important region in the future.

Sensitivity to changing sea ice conditions

Because the NCP was so tightly coupled to the number of open water days in the ASP, it is important to consider the ASP within the context of historic (Stammerjohn et al., 2015) and future changes in the sea ice cover for the region. The Amundsen Sea embayment is part of the larger western Antarctic region experiencing long-term (1979–2014) losses in annual ice season duration. In the ASP region in particular,

open water duration has increased by nearly 50 days since 1979, primarily driven by earlier opening in the spring. The area-averaged mean day of sea ice retreat (< 15%) has shifted from Day 398 ± 7 to Day 353 ± 12. A quick comparison to the sampling dates of ASPIRE (Table 1) confirms that, on average, none of the 13 ASPIRE stations would have been ice-free in 1979–80 at the time of year we sampled them in 2010–11. It is likely then, that primary production and export in the ASP region are much higher in December than was the case several decades ago. Whether productivity overall has increased over the entire open water season, or just shifted in time, is unknown. Satellite analyses show that interannual variability is high and no secular trend in total annual production was detectable from 1997 to 2014 (Arrigo et al., 2012, 2015). The fate of the bloom may have changed recently, however. Although we have attributed the modest mesozooplankton bloom response in our observations to the dominance of *Phaeocystis*, a climate-driven phenological mismatch between phytoplankton and grazers may also be at play (Wassmann, 2011); e.g., earlier ice break-up may be favoring specific phytoplankton or outpacing the zooplankton response. Regional sediment or ice-core records going back further in time could be of some use here.

Looking forward, an even earlier opening would enhance productivity only if light and nutrients were adequate to support phytoplankton. Clearly, light and iron were adequate for the bloom during December 2010 in the ASP region (Alderkamp et al., 2015; Schofield et al., 2015). Whether a progressively earlier opening will stimulate production further is unknown. As observed in the west Antarctic Peninsula (see, for example, Montes-Hugo et al., 2009), the total loss of sea ice and marginal ice zone conditions can lead to deeper mixed layers, greater light limitation, and severe declines in NCP. Any enhancement in productivity that we may have observed in response to the early stages of climate change is not likely sustainable in the long term if the sea ice continues to disappear.

Conclusions

The Amundsen Sea hosts the most productive polynya in all of coastal Antarctica, with its vibrant green waters (> 20 μg Chl *a* L^{-1}) and high primary productivity (> 200 mmol C m^{-2} d^{-1}) leading to high early season net community production (up to 6 mol C m^{-2}), an efficient biological pump, and carbon export (up to 75 mmol C m^{-2} d^{-1}). During ASPIRE, in austral summer 2010–11, we aimed to determine physical and biological mechanisms driving the production and fate of this extraordinary algal bloom, with an eye towards predicting how this system will respond to further change. What we found was an extreme phytoplankton bloom dominated by *Phaeocystis antarctica*, supported by stratification provided by seasonal sea ice melt, abundant wintertime surface nitrate (> 30 μmol L^{-1}), and an iron flux associated with the nearby melting ice sheets. Here, we show that a surprisingly high fraction (up to 62%) of the seasonal net community production was exported to sub-euphotic depths during the high bloom conditions, in the absence of significant grazing from mesozooplankton, although microbial remineralization in the mid-depths reduced export to the bottom. With both high export quantities and high biological pump efficiency, the ASPIRE ecosystem stands apart from most other ocean biological pumps, reflecting significant release from both iron and light limitation. This globally significant biological pump is clearly linked to climate-sensitive changes in both sea ice cover and nearby ice shelves, but the carbon cycle feedbacks to climate may not be sustainable, particularly if sea ice continues to disappear from the region.

References

Alderkamp A-C, Dijken GL, Lowry KE, Connelly TL, Lagerstrom M, et al. 2015. Fe availability drives phytoplankton photosynthesis rates during spring bloom in the Amundsen Sea Polynya, Antarctica. *Elem Sci Anth* **2**: 000043 doi: 10.12952/journal.elementa.000043.

Alderkamp AC, Mills MM, Van Dijken GL, Laan P, Thuyróczy CE, et al. 2012. Iron from melting glaciers fuels phytoplankton blooms in the Amundsen Sea (Southern Ocean): Phytoplankton characteristics and productivity. *Deep-Sea Res Pt II* **71–76**: 32–48. doi: 10.1016/j.dsr2.2012.03.005.

Alkire MB, D'Asaro E, Lee C, Perry MJ, Gray A, et al. 2012. Estimates of net community production and export using high-resolution Lagrangian measurements of O_2, NO_3^-, and POC through the evolution of a spring diatom bloom in the North Atlantic. *Deep-Sea Res Pt I* **64**: 157–174.

Armstrong FAJ, Stearns CR, Strickland JDH. 1967. The measurement of upwelling and subsequent biological processes by means of the Technicon AutoAnalyzer ™ and associated equipment. *Deep-Sea Res* **14**(3): 381–389.

Armstrong RA, Peterson ML, Lee C, Wakeham SG. 2009. Settling velocity sprectra and the ballast ratio hypothesis. *Deep-Sea Res Pt II* **56**: 1470–1478.

Arrigo KR, Lowry KE, van Dijken GL. 2012. Annual changes in sea ice and phytoplankton in polynyas of the Amundsen Sea, Antarctica. *Deep-Sea Res Pt II* **71–76**: 5–15. doi: 10.1016/j.dsr2.2012.03.006.

Arrigo KR, Robinson DH, Worthen DL, Dunbar RB, DiTullio GR, et al. 1999. Phytoplankton community structure and the drawdown of nutrients and CO_2 in the Southern Ocean. *Science* **283**: 365–367.

Arrigo KR, van Dijken GL, Bushinsky S. 2008. Primary production in the Southern Ocean, 1997–2006. *J Geophys Res* **113**: C08004. doi: 10.1029/2007JC004551.

Arrigo KR, van Dijken GL, Strong A. 2015. Environmental controls of marine productivity hot-spots around Antarctica. *J Geophys Res* **120**(8): 5545–5565. doi: 10.1002/2015JC010888.

Arrigo KR, van Dijken GL. 2003. Phytoplankton dynamics within 37 Antarctic coastal polynya systems. *J Geophys Res* **108**: 3271. doi: 10.1029/2002JC001739.

Arrigo KR, van Dijken GL. 2004. Annual cycles of sea ice and phytoplankton in Cape Bathurst polynya, southeastern Beaufort Sea, Canadian Arctic. *Geophys Res Let* **31**(8): L08304. doi: 10.1029/2003GL018978.

Ashjian CJ, Smith S, Bignami F, Hopkins T, Lane P. 1997. Distribution of zooplankton in the Northeast Water Polynya during summer 1992. *J Mar Syst* **10**: 279–298.

Atkinson A, Shreeve RS, Pakhomov EA, Priddle J, Blight SP, et al. 1996. Zooplankton response to a phytoplankton bloom near South Georgia, Antarctic. *Mar Ecol-Prog Ser* **144**:195–210.

Atlas EL, Hager SW, Gordon LI, Park PK. 1971. A practical manual for use of the Technicon Autoanalyzer™ in seawater nutrient analyses; revised. *Technical Report 215 - Ref. No. 71-22. 48 pp*. Oregon State University, Dept of Oceanography.

Bates NR, Best MHP, Hansell DA. 2005. Spatio-temporal distribution of dissolved inorganic carbon and net community production in the Chukchi and Beaufort Seas. *Deep-Sea Res Pt II* **52**: 3303–3323.

Bauerfeind E, Nöthig EM, Beszczynska A, Fahl K, Kaleschke L, et al. 2009. Particle sedimentation patterns in the eastern Fram Strait during 2000–2005: Results from the Arctic long-term observatory HAUSGARTEN. *Deep-Sea Res Pt I* **56**: 1471–1487.

Beaulieu SE. 2002. Accumulation and fate of phytodetritus on the sea floor, in Atkinson RJA, Barnes M, eds., *Oceanography and Marine Biology: An Annual Review*. Volume **40**: pp. 171–232. doi: 10.1201/9780203180594.ch4.

Behrenfeld MJ, Falkowski PG. 1997. Photosynthetic rates derived from satellite-based chlorophyll concentration. *Limnol Oceanogr* **42**: 1–20.

Berelson WM. 2001. The flux of particulate organic carbon into the ocean interior: A comparison of four U.S. JGOFS regional studies. *Oceanography* **14**(4): 59–67.

Bernard KS, Steinberg DK, Schofield OME. 2012. Summertime grazing impact of the dominant macrozooplankton off the western Antarctic Peninsula. *Deep-Sea Res Pt I* **62**:111–122.

Bernhardt H, Wilhelms A. 1967. The continuous determination of low level iron, soluble phosphate and total phosphate with the AutoAnalyzer. *Technicon Symp., Vol. I, p. 386*.

Bevington PT. 1969. *Data reduction and error analysis for the physical sciences*. McGraw-Hill: New York. 336 pp.

Bjørnsen PK, Kuparinen J. 1991. Determination of bacterioplankton biomass, net production and growth efficiency in the Southern Ocean. *Mar Ecol-Prog Ser* **71**: 185–194.

Børsheim KY, Bratbak G. 1987. Cell volume to cell carbon conversion factors for bacterivorous ***Monas*** sp. enriched from seawater. *Mar Ecol-Prog Ser* **36**: 171–175.

Boyd PW, Trull TW. 2007. Understanding the export of biogenic particles in oceanic waters: Is there a consensus? *Progr Oceanogr* **72**(4): 276–312.

Brown PJ, Jullion L, Landscützer P, Bakker DCE, Garabato ACN, et al. 2015. Carbon dynamics of the Weddell Gyre, Southern Ocean. *Global Biogeochem Cy* **29**: 288–306. doi: 10.1002/2014GB005006.

Brzezinski MA. 1985. The Si:C:N ratio of marine diatoms: interspecific variability and the effect of some environmental variables. *J Phycology* **21**(3): 347–357.

Buesseler KO, Boyd PW. 2009. Shedding light on processes that control particle export and flux attenuation in the twilight zone of the open ocean. *Limnol Oceanogr* **54**(4): 1210–1232. doi: 10.4319/lo.2009.54.4.1210.

Calbert A, Atenza D, Broglio E, Alcaraz M, Vaque D. 2006. Trophic ecology of *Calanoides acutus* in Gerlach Strait and Bellinghausen Sea Watrs (Antactica, December 2002). *Polar Biol* **29**: 510–518.

Caron DA, Dennett MR, Lonsdale DJ, Moran DM, Shalapyonok L. 2000. Microzooplankton herbivory in the Ross Sea, Antarctica. *Deep-Sea Res Pt II* **47**:3249–3272.

Chen M, Huang Y, Guo L, Cai P, Yang W, et al. 2002. Biological productivity and carbon cycling in the Arctic Ocean. *Chinese Sci Bull* **47**(12): 1037–1040. doi: 10.1007/BF02907578.

Chen M, Liu H. 2011. Experimental simulation of trophic interactions among omnivorous copepods, heterotrophic dinoflagellates and diatoms. *J Exp Mar Biol Ecol* **403**:65–74.

Christaki U, Courties C, Massana R, Catala P, Lebaron P, et al. 2011. Optimized routine flow cytometric enumeration of heterotrophic flagellates using SYBR Green I. *Limnol Oceanogr: Methods* **9**: 329–339.

Cisewski B, Strass VH, Losch M, Prandke H. 2008. Mixed layer analysis of a mesoscale eddy in the Antarctic Polar Front Zone. *J Geophys Res-Oceans* **113**: C05017. doi: 10.1029/2007JC004372.

Collier R, Dymond J, Honjo S, Manganini S, Francois R, et al. 2000. The vertical flux of biogenic and lithogenic material in the Ross Sea: moored sediment trap observations 1996–1998. *Deep-Sea Res Pt II* **47**: 3491–3520. doi: 10.1016/S0967-0645(00)00076-X.

Collins JR, Edwards BR, Thamatrakoln K, Ossolinski JE, DiTullio GR, et al. 2015. The multiple fates of sinking particles in the North Atlantic Ocean. *Global Biogeochem Cy* **29**: 1471–1494. doi: 10.1002/2014GB005037.

Cooley SR, Yager PL. 2006. Physical and biological contributions to the western tropical North Atlantic Ocean carbon sink formed by the Amazon River plume. *J Geophys Res* **111**: C08018. doi: 10.1029/2005JC002954.

Dam HG, Peterson WT. 1988. The effect of temperature on the gut clearance rate constant of planktonic copepods. *J Exp Mar Biol Ecol* **123**: 1–14.

Deibel D, Daly KL. 2007. Zooplankton processes in Arctic and Antarctic polynyas, in Smith Jr WO Jr, Barber D, eds., *Polynyas: Windows into Polar Oceans*. (Elsevier Oceanography Series, 74): pp. 271–322.

Delmont TO, Eren AM, Vineis JH, Post AF. 2015. Genome reconstructions indicate the partitioning of ecological functions inside a phytoplankton bloom in the Amundsen Sea, Antarctica. *Front Microbiol* **6**:1090. doi: 10.3389/fmicb.2015.01090.

Delmont TO, Hammar KM, Ducklow HW, Yager PL, Post AF. 2014. ***Phaeocystis antarctica*** blooms strongly influence bacterial community structures in the Amundsen Sea polynya. *Front Microbiol* **5**:646. doi: 10.3389/fmicb.2014.00646.

Dickson AG, Afghan JD, Anderson GC. 2003. Reference materials for oceanic CO_2 analysis: a method for the certification of total alkalinity. *Mar Chem* **80**: 185–197.

Dickson AG, Sabine CL, Christian JR, eds. 2007. Guide to best practices for ocean CO_2 measurements. *PICES Special Publication 3: 191 pp*. http://cdiac.ornl.gov/oceans/Handbook_2007.html.

DiTullio GR, Grebmeier JM, Arrigo KR, Lizotte MP, Robinson DH, et al. 2000. Rapid and early export of ***Phaeocystis antarctica*** blooms in the Ross Sea, Antarctica. *Nature* **404**: 595–598.

Ducklow HW, Steinberg DK, Buesseler KO. 2001. Upper ocean carbon export and the biological pump. *Oceanography* **14**(4): 50–58.

Ducklow HW, Wilson SE, Post AF, Stammerjohn SE, Erickson M, et al. 2015. Particle flux on the continental shelf in the Amundsen Sea Polynya and Western Antarctic Peninsula. *Elem Sci Anth* **3**: 000046 doi: 10.12952/journal.elementa.000046.

Emerson S. 2014. Annual net community production and the biological carbon flux in the ocean. *Global Biogeochem Cy* **28**: 14–28. doi: 10.1002/2013GB004680.

EPA. 1984. Methods for Chemical Analysis of Water and Wastes, March 1984. *EPA-600/4-79-020, "Nitrogen Ammonia", Method 350.1 (Colorimetric, Automated Phenate)*.

Eppley RW. 1989. New production: history, methods, problems, in Berger WH, Smetacek VS, Wefer G, eds., *Productivity of the Ocean: Present and Past*. New York: Wiley & Sons: pp. 85–97.

Forest A, Stemmann L, Picheral M, Burdorf L, Robert D, et al. 2012. Size distribution of particles and zooplankton across the shelf-basin system in southeast Beaufort Sea: Combined results from an Underwater Vision Profiler and vertical net tows. *Biogeosciences* **9**: 1301–1320.

Fransson A, Chierici M, Yager PL, Smith Jr WO. 2011. Antarctic sea ice carbon dioxide system and controls. *J Geophys Res* **116** (C12). doi: 10.1029/2010JC006844.

Fransz HG, Gonzalez SR. 1997. Latitudinal metazoan plankton zones in the Antarctic circumpolar current along 6 W during austral spring 1992. *Deep-Sea Res Pt II* **44**: 395–414.

Froneman P, Perissinoto R. 1996. Microzooplankton grazing in the southern ocean: Implications for the carbon cycle. *Marine Ecol-P S Z N I* **17**: 99–115.

Froneman PW, Balarin MG. 1998. Structure and grazing impact of the protozooplankton community in the waters surrounding the Prince Edward Islands (Southern Ocean). *Polar Biol* **20**:198–205.

Froneman PW. 2004. Protozooplankton community structure and grazing impact in the eastern Atlantic sector of the Southern Ocean in austral summer 1998. *Deep-Sea Res Pt II* **51**: 2633–2643.

Frost BW. 1984. Utilization of phytoplankton production in the surface layer. *Global Ocean Flux Study: Proceedings of a Workshop, September 10–14, 1984, Woods Hole, Massachusetts*. Washington, D.C.: National Academy Press: pp. 125–135.

Gallienne CP, Robins DB, Woodd-Walker RS. 2001. Abundance, distribution and size structure of zooplankton along a 20° west meridional transect of the North East Atlantic Ocean in July. *Deep-Sea Res Pt II* **48**: 925–950.

Goswami SC. 2004. Zooplankton methodology, collection & identification - A field manual. Dona Paula, Goa: National Institute of Oceanography: 26 pp.

Grebmeier JM, Barry JP. 2007. Benthic Processes in Polynyas, in Smith Jr WO Jr, Barber D, eds., *Polynyas: Windows into Polar Oceans.* Elsevier/CRC: New York: pgs. 363–390.

Hansell DA, Carlson CA, Repeta DJ, Schlitzer R. 2009. Dissolved organic matter in the ocean: A controversy stimulates new insights. *Oceanography* **22**(4): 202–211. doi: 10.5670/oceanog.2009.109.

Hedges JI, Stern JH. 1984. Carbon and nitrogen determinations of carbonate-containing solids. *Limnol Oceanogr* **29**(3): 657–663.

HELCOM. 2014. A manual for marine monitoring in the COMBINE programme of HELCOM. http://helcom.fi/Lists/Publications/Manual%20for%20Marine%20Monitoring%20in%20the%20COMBINE%20Programme%20of%20HELCOM.pdf.

Herndl GJ, Reinthaler T. 2013. Microbial control of the biological pump. *Nature Geosci* **6**: 718: 724.

Hoppema M, Fahrbach E, Stoll MHC, de Baar HJW. 1999. Annual uptake of atmospheric CO_2 by the Weddell Sea derived from a surface lay balance, including estimation of entrainment and new production. *J Mar Syst* **19**: 219–233.

Huang K, Ducklow H, Vernet M, Cassar N, Bender ML. 2012. Export production and its regulating factors in the West Antarctica Peninsula region of the Southern Ocean. *Global Biogeochem Cy* **26**: GB2005. doi: 10.1029/2010GB004028.

Huntley M, Zhou M. 2000. US JGOFS Data System: Southern Ocean zooplankton displacement volumes from MOCNESS tows. U.S. JGOFS. http://usjgofs.whoi.edu/jg/serv/jgofs/southern/ nbp96 4A/dv mocness.html0, and http://usjgofs.whoi.edu/jg/ serv/jgofs/southern/nbp97 1/dv mocness.html0.

Jacobs SS, JC Comiso. 1997. Climate variability in the Amundsen and Bellingshausen Seas. *J Climate* **10**(4): 697–709.

Jensen HM, Pedersen L, Burmeister AD, Hansen BW. 1999. Pelagic primary production during summer along 65 to 72°N off West Greenland. *Polar Biol* **21**(5): 269–278. doi: 10.1007/s003000050362.

Johnson KM, Wills KD, Butler DB, Johnson WK, Wong CS. 1993. Coulometric total carbon dioxide analysis for marine studies: Maximizing the performance of an automated gas extraction system and coulometric detector. *Mar Chem* **44** : 167–187.

Joughin I, Smith BE, Medley B. 2014. Marine ice sheet collapse potentially underway for the Thwaites Glacier basin, West Antarctica. *Science* **344**: 735–738.

Karl DM, Christian JR, Dore JE, Hebel DV, Letelier RM, et al. 1996. Seasonal and interannual variability in primary production and particle flux at station ALOHA. *Deep-Sea Res* **43**: 539–568.

Karl DM. 1993. Microbial processes in the Southern Ocean, in Friedmann EI, ed., *Antarctic Microbiology*. Wiley, New York, pp. 1–63.

Kellogg CTE, Carpenter SD, Renfro AA, Sallon A, Michel C, et al. 2011. Evidence for microbial attenuation of particle flux in the Amundsen Gulf and Beaufort Sea: Elevated hydrolytic enzyme activity on sinking aggregates. *Polar Biol* **34**(12): 2007–2023, doi: 10.1007/s00300-011-1015-0.

Knap A, Michaels A, Close A, Ducklow H, Dickson A. 1996. Protocols for the Joint Global Ocean Flux Study (JGOFS) core measurements. *JGOFS Report No. 19, vi+170 pp. Reprint of the IOC Manuals and Guides No. 29, UNESCO 1994*.

Knauer GA, Martin JH, Bruland KW. 1979. Fluxes of particulate carbon, nitrogen, and phosphorus in the upper water column of the northeast Pacific. *Deep-Sea Res* **26**: 97–108.

Landry MR, Calbet A. 2004. Microzooplankton production in the oceans. *ICES J Mar Sci* **61**: 501–507.

Le Moigne FAC, Poulton AJ, Henson SA, Daniels CJ, Fragoso GM, et al. 2015. Carbon export efficiency and phytoplankton community composition in the Atlantic sector of the Arctic Ocean, *J Geophys Res: Oceans* **120**: 3896–3912. doi: 10.1002/2015JC010700.

Lee DB, Choi KH, Ha HK, Yang EJ, Lee SH, et al. 2013. Mesozooplankton distribution patterns and grazing impacts of copepods and ***Euphausia crystalloropohias*** in the Amundsen Sea, West Antarctica, during austral summer. *Polar Biol* **36**: 1215–1230.

Lowry KE, Pickart RS, Mills MM, Brown ZW, Van Dijken GL, et al. 2015. The influence of winter water on phytoplankton blooms in the Chukchi Sea. *Deep-Sea Res Pt II* **118**: 53–72.

Luchetta A, Lipizer M, Socal G. 2000. Temporal evolution of primary production in the central Barents Sea. *J Mar Syst* **27**:177–193.

Mackey MD, Mackey DJ, Higgins HW, Wright SW. 1996. CHEMTAX- a program for estimating class abundances from chemical markers: application to HPLC measurements of phytoplankton. *Mar Ecol-Prog Ser* **144**: 265–283.

Marie D, Partensky F, Jacquet S, Vaulot D. 1997. Enumeration and cell cycle analysis of natural populations of marine picoplankton by flow cytometry using the nucleic acid stain SYBR Green I. *Appl Environ Microb* **63**: 186–193.

Martin JH, Knauer GA, Karl DM, Broenkow WW. 1987. VERTEX: Carbon cycling in the NE Pacific. *Deep-Sea Res* **34**: 267–285.

Mei ZP, Legendre L, Gratton Y, Tremblay JE, LeBlanc B, et al. 2003. Phytoplankton production in the North Water Polynya: size-fractions and carbon fluxes, April to July 1998. *Mar Ecol-Prog Ser* **256**: 13–27. doi: 10.3354/meps256013.

Menden-Deuer S, Lessard EJ. 2000. Carbon to volume relationships for dinoflagellates, diatoms, and other protist plankton. *Limnol Oceanogr* **45**: 569–579.

Metzl N, Tilbrook B, Poisson A. 1999. The annual fCO_2 cycle and the air-sea CO_2 flux in the sub-Antarctic Ocean. *Tellus* **51B**: 849–861.

Miller LA, DiTullio GR. 2007. Gas fluxes and dynamics in polynyas, in Smith Jr WO, Barber D, eds., *Polynyas: Windows into Polar Oceans*. (Elsevier Oceanography Series, 74): Pp. 165–192.

Miller LA, Yager PL, Erickson KA, Amiel D, Bâcle J, et al. 2002. Carbon distributions and fluxes in the North Water, 1998 and 1999. *Deep-Sea Res Pt II* **29**: 5151–5170.

Montes-Hugo M, Doney SC, Ducklow HW, Fraser W, Martinson D, et al. 2009. Recent changes in phytoplankton communities associated with rapid regional climate change along the western Antarctic Peninsula. *Science* **323**: 1470–1473.

Moore CM, Mills MM, Arrigo KR, Berman-Frank I, Bopp L, et al. 2013. Processes and patterns of oceanic nutrient limitation. *Nature Geosci* **6**: 701–710. doi: 10.1038/NGEO1765.

Mouginot J, Rignot E, Scheuchl B. 2014. Sustained increase in ice discharge from the Amundsen Sea Embayment, West Antarctica, from 1973–2013. *Geophys Res Lett* **41**: doi: 10.1002/2013GL059069.

Mu L, Stammerjohn SE, Lowry KE, Yager PL. 2014. Spatial variability of surface pCO_2 and air-sea CO_2 flux in the Amundsen Sea Polynya, Antarctica. *Elem Sci Anth* **2**: 000036. doi: 10.12952/journal.elementa.000036.

Munson KM, Lamborg CH, Swarr GJ, Saito MA. 2015. Mercury Species Concentrations and Fluxes in the Central Tropical Pacific Ocean. *Global Biogeochem Cy* **29**(5): 656–676.

Nejstgaard JC, Tang KW, Steinke M, Dutz J, Koski M, et al. 2007. Zooplankton grazing on ***Phaeocystis***: A quantitative review and future challenges. *Biogeochemistry* **83**:147–172.

Nitsche FO, Jacobs SS, Larter RD, Gohl K. 2007. Bathymetry of the Amundsen Sea continental shelf: Implications for geology, oceanography, and glaciology. *Geochem Geophys Geosyst* **8**: 1–10. doi: 10.1029/2007gc001694.

Pakhomov EA, Froneman PW. 2004. Zooplankton Dynamics in the eastern Atlantic sector of the Southern Ocean during the austral summer 1997/1998 – Part 2: Grazing Impact. *Deep-Sea Res Pt II* **51**: 2617–2631.

Patton CJ. 1983. Design, characterization and applications of a miniature continuous flow analysis system [Ph.D. Thesis]. Ann Arbor, Mich.: Michigan State University, U. Microfilms International. 150 pp.

Planquette H, Sherrell RM, Stammerjohn S, Field MP. 2013. Particulate iron delivery to the water column of the Amundsen Sea, Antarctica. *Mar Chem* **153**: 15–30. doi: 10.1016/j.marchem.2013.04.006.

Planquette H, Sherrell RM. 2012. Sampling for particulate trace element determination using water sampling bottles: Methodology and comparison to in situ pumps. *Limnol Oceanogr: Methods* **10**: 367–388.

Porter KG, Feig YS. 1980. The use of DAPI for identifying and counting aquatic microflora. *Limnol Oceanogr* **25**(5): 943–948.

Prézelin BB, Hofmann EE, Mengelt C, Klinck JM. 2000. The linkage between upper Circumpolar Deep Water (UCDW) and phytoplankton assemblages on the west Antarctic Peninsula continental shelf. *J Mar Res* **58**: 165–202. doi: 10.1357/002224000321511133.

Quay PD, Peacock C, Björkman K, Karl DM. 2010. Measuring primary production rates in the ocean: Enigmatic results between incubation and non-incubation methods at Station ALOHA. *Global Biogeochem Cy* **24**: GB3014.

Randall-Goodwin E, Meredith MP, Jenkins A, Yager PL, Sherrell RM, et al. 2015. Freshwater distributions and water mass structure in the Amundsen Sea Polynya region, Antarctica. *Elem Sci Anth* **3**: 000065. doi: 10.12952/journal.elementa.000065.

Redfield AC, Ketchum BH, Richards FA. 1963. The influence of organisms on the composition of seawater, in Hill MN, ed., *The Sea*. Vol. **2**. New York: Interscience. pp 26–77.

Reigstad M, Wassmann P. 2007. Does ***Phaeocystis*** spp. contribute significantly to vertical export of organic carbon? *Biogeochem* **83**(1–3): 217–234. doi: 10.1007/s10533-007-9093-3.

Robertson R. 2013. Tidally induced increases in melting of Amundsen Sea ice shelves. *J Geophys Res: Oceans* **118**: 3138–3145. doi: 10.1002/jgrc.20236.

Rysgaard S, Mortensen J, Juul-Pedersen T, Sørensen LL, Lennert K, et al. 2011. High air–sea CO2 uptake rates in nearshore and shelf areas of Southern Greenland: Temporal and spatial variability. *Mar Chem* **128–129**: 26–33. doi: 10.1016/j.marchem.2011.11.002.

Sarmiento JL, Dunne J, Armstrong RA. 2004. Do we now understand the ocean's biological pump? *US JGOFS News 12: 1–5*.

Sarmiento JL, Toggweiler JF. 1984. A new model for the role of the oceans in determining atmospheric pCO_2. *Nature* **308**: 621–624. doi: 10.1038/308621a0.

Saunders PA, Deibel D, Stevens CJ, Rivkin RB, Lee S-H. 2003. Fate of sinking particles, especially fecal pellets, within the epipelagic zone in the North Water (NOW) polynya of northern Baffin Bay. *Mar Ecol-Prog Ser* **278**: 17–25.

Schlitzer R. 2002. Carbon export fluxes in the Southern Ocean: results from inverse modeling and comparison with satellite-based estimates. *Deep-Sea Res Pt II* **49**(9–10): 1623–1644.

Schofield O, Miles T, Alderkamp A, Lee S, Haskins C, et al. 2015. In situ phytoplankton distributions in the Amundsen Sea Polynya measured by autonomous gliders. *Elem Sci Anth* **3**: 000073 . doi: 10.12952/journal.elementa.000073.

Sherrell RM, Lagerström M, Forsch KO, Stammerjohn SE, Yager PL. 2015. Dynamics of dissolved iron and other bioactive trace metals (Mn, Ni, Cu, Zn) in the Amundsen Sea Polynya, Antarctica. *Elem Sci Anth* **3**: 000071. doi: 10.12952/journal.elementa.000071.

Sieburth JMcN. 1959. Antibacterial activity of antarctic marine phytoplankton. *Limnol Oceanogr* **4**: 419–424.

Sieburth JMcN. 1960. Acrylic acid, an 'antibiotic' principle in ***Phaeocystis*** blooms in antarctic waters. *Science* **132**: 676–677.

Sieburth JMcN. 1961. Antibiotic properties of acrylic acid, a factor in the gastrointestinal antibiosis of polar marine animals. *J Bacteriol* **82**: 72–79.

Sigman DM, Hain MP, Haug GH. 2010. The polar ocean and glacial cycles in atmospheric CO_2 concentration. *Nature* **466**: 47–55. doi: 10.1038/nature09149.

Sigman DM, Hain MP. 2012. The biological productivity of the ocean. *Nature Education Knowledge* **3**(10): 21.

Simon M, Azam F. 1989. Protein content and protein synthesis rates of planktonic marine bacteria. *Mar Ecol-Prog Ser* **51**: 201–213.

Sipler RE, Connelly TL. 2015. Bioavailability of surface dissolved organic matter to aphotic bacterial communities in the Amundsen Sea Polynya, Antarctica. *Elem Sci Anth* **3**: 000060 doi: 10.12952/journal.elementa.000060.

Slaughter AM, Bollens SM, Bollens GR. 2006. Grazing impact of mesozooplankton in an upwelling region off northern California, 2000–2003. *Deep Sea Res Pt II* **53**: 3099–3115.

Smith Jr WO, Barber DG, eds. 2007. *Polynyas: Windows to the World*. Elsevier Oceanography Series, vol. 74, Elsevier Science, Amsterdam, 474 pp.

Smith Jr WO, Carlson CA, Ducklow HW, Hansell DA. 1998. Growth dynamics of ***Phaeocystis antarctica***-dominated plankton assemblages from the Ross Sea. *Mar Ecol-Progr Ser* **168**: 229–244.

Smith Jr WO, Codispoti LA, Nelson DM, Manley T, Buskey EJ, et al. 1991. Importance of ***Phaeocystis*** blooms in the high-latitude ocean carbon cycle. *Nature* **352**: 514–516.

Smith Jr WO. 1995. Primary productivity and new production in the Northeast Water (Greenland) Polynya during summer 1992. *J Geophys Res: Oceans* **100** (C3): 4357–4370. doi: 10.1029/94JC02764.

Sokal RR, Rohlf FJ. 1981. *Biometry. The Principles and Practice of Statistics in Biological Research, 2nd edition.* New York: WH Freeman and Company: 859 pp.

St Laurent P, Klinck JM, Dinniman MS. 2015. Impact of local winter cooling on the melt of Pine Island Glacier, Antarctica. *J Geophys Res: Oceans* **120**(10): 6718–6732. doi: 10.1002/2015JC010709.

Stammerjohn SE, Maksym T, Massom RA, Lowry KE, Arrigo KR, et al. 2015. Seasonal sea ice changes in the Amundsen Sea, Antarctica, over the period of 1979–2014. *Elem Sci Anth* **3**: 000055. doi: 10.12952/journal.elementa.000055.

Steeman-Nielsen E. 1952. The use of radioactive carbon (^{14}C) for measuring organic production in the sea. *J Conseil* **18**: 117–140.

Steinberg DK, Carlson CA, Bates NR, Goldthwait SA, Madin LP, et al. 2000. Zooplankton vertical migration and the active transport of dissolved organic and inorganic carbon in the Sargasso Sea. *Deep-Sea Res Pt I* **47**: 137–158.

Steinberg DK, Van Mooy BAS, Buesseler KO, Boyd PW, Kobari T, et al. 2008. Bacterial vs. zooplankton control of sinking particle flux in the ocean's twilight zone. *Limnol Oceanogr* **53**(4): 1327–1338.

Stoecker DK, Gifford DJ, Putt M. 1994. Preservation of marine planktonic ciliates: losses and cell shrinkage during fixation. *Mar Ecol-Prog Ser* **110**: 293–299.

Straile D. 1997. Gross growth efficiencies of protozoan and metazoan zooplankton and their dependence on food concentration, predator-prey weight ratio, and taxonomic group. *Limnol Oceanogr* **4**: 1375–1385.

Strickland JDH, Parsons TR. 1972. A Practical Handbook of Seawater Analysis. 2nd edition. *Bull Fish Res Bd Can* **167**:1–310.

Sunda WG, Huntsman SA. 1998. Processes regulating cellular metal accumulation and physiological effects: phytoplankton as model systems. *Sci Total Environ* **219**: 165–181.

Sweeney C, Hansell DA, Carlson CA, Codispoti LA, Gordon LI, et al. 2000. Biogeochemical regimes, net community production and carbon export in the Ross Sea, Antarctica. *Deep-Sea Res Pt II* **47**(15–16): 3369–3394.

Tagliabue A, Arrigo KR. 2003. Anomalously low zooplankton abundance in the Ross Sea: An alternative explanation. *Limnol Oceanogr* **48**(2): 686–699.

Takahashi T, Sutherland SC, Sweeney C, Poisson A, Metzl N, et al. 2002. Global sea-air CO_2 flux based on climatological surface ocean pCO_2, and seasonal biological and temperature effects. *Deep-Sea Res Pt II* **49**(9–10): 1601–1622.

Takahashi T, Sutherland SC, Wanninkhof R, Sweeney C, Feely RA, et al. 2009. Climatological mean and decadal change in surface ocean pCO_2, and net sea-air CO_2 flux over the global oceans. *Deep-Sea Res Pt II* **56**: 554–577.

Thomas DN, Dieckmann GS, eds. 2010. *Sea Ice: An introduction to its physics, chemistry, biology and geology*. Oxford, U.K.: Wiley-Blackwell: 621 pp.

Tréguer PJ, De La Rocha CL. 2013. The world ocean silica cycle. *Annu Rev Mar Sci* **5**:477–501. doi: 10.1146/annurev-marine-121211-172346.

Tremblay JE, Gratton Y, Fauchot J, Price NM. 2002. Climatic and oceanic forcing of new, net, and diatom production in the North Water Polynya. *Deep-Sea Res Pt II* **49**: 4927–4946.

Tremblay JE, Robert D, Varela DE, Lovejoy C, Darnis G, et al. 2012. Current state and trends in Canadian Arctic marine ecosystems: I. Primary production. *Clim Change* **115**: 161–178, doi: 10.1007/s10584-012-0496-3.

Tremblay JE, Smith Jr WO. 2007. Primary production and nutrient dynamic in polynyas, in Smith Jr WO, Barber D, eds., *Polynyas: Windows into Polar Oceans*. (Elsevier Oceanography Series, 74): pp. 239–269.

Trudnowska E, Basedow SL, Blachowiak-Samolyk K. 2014. Mid-summer mesozooplankton biomass, its size distribution, and estimated production within a glacial Arctic fjord (Hornsund, Svalbard). *J Mar Syst* **137**: 55–56.

Turner JT. 2015. Zooplankton fecal pellets, marine snow, phytodetritus and the ocean's biological pump. *Progr Oceanogr* **130**: 205–248. doi: 10.1016/j.pocean.2014.08.005.

Tynan CT. 1998. Ecological importance of the southern boundary of the Antarctic Circumpolar Current. *Nature* **392**: 708–710.

Vaqué D, Guixa-Boixereu N, Gasol JM, Pedrós-Alió C. 2002. Distribution of microbial biomass and importance of protists in regulating prokaryotic assemblages in three areas close to the Antarctic Peninsula in spring and summer 1995/96. *Deep-Sea Res Pt II* **49**: 847–867.

Ward P, Atkinson A, Murray AWA, Wood AG, Williams R, et al. 1995. The summer zooplankton community at South Georgia: Biomass, vertical migration and grazing. *Polar Biol* **15**: 195–208.

Wassmann P, Vernet M, Mitchell BG, Rey F. 1990. Sedimentation of ***Phaeocystis pouchettii*** in the Barents Sea. *Mar Ecol-Prog Ser* **66**: 183–195.

Wassmann P. 1993. Significance of sedimentation for the termination of ***Phaeocystis*** blooms. *J Mar Syst* **5**: 81–100.

Wassmann P. 1998. Retention versus export food chains: processes controlling sinking loss from marine pelagic systems. *Hydrobiologia* **363**: 29–57.

Wassmann P. 2011. Arctic marine ecosystems in an era of rapid climate change. *Progr Oceanogr* **90**: 1–17. doi: 10.1016/j.pocean.2011.02.002

Williams CM, Dupont AM, Loevenich J, Post AF, Dinasquet J, et al. 2016. Pelagic microbial heterotrophy in response to a highly productive bloom of ***Phaeocystis antarctica*** in the Amundsen Sea Polynya, Antarctica. *Elem Sci Anth* **4**(1): 000102.

Wilson SE, Swalethorp R, Kjellerup S, Wolverton MA, Ducklow HW, et al. 2015. Meso- and macro-zooplankton community structure of the Amundsen Sea Polynya, Antarctica (Summer 2010–2011). *Elem Sci Anth* **3**: 000033.

Wong APS, Bindoff NL, Forbes A. 1998. Ocean-ice shelf interaction and possible bottom water formation in Prydz Bay, Antarctica. Ocean, Ice, and Atmosphere: Interactions at the Antarctic Continental Margin. *Antarct Res Ser* **75**: 173–187.

World Ocean Atlas. 2001. Online data repository at National Ocean Data Center. National Oceanic and Atmospheric Administration. http://www.nodc.noaa.gov/OC5/WOA01/woa01dat.html.

Wright SW, Jeffrey S, Mantoura R, Lewellyn C, Bjornland C, et al. 1991. An improved HPLC method for the analysis of chlorophylls and carotenoids from marine phytoplankton. *Mar Ecol-Prog Ser* **77**: 183–196.

Wright SW, Thomas DP, Marchant HJ, Higgins HW, Mackey MD, et al. 1996. Analysis of phytoplankton of the Australian sector of the Southern Ocean: Comparisons of microscopy and size frequency data with interpretations of pigment HPLC data using the 'CHEMTAX' matrix factorisation program. *Mar Ecol-Prog Ser* **144**: 285–298.

Wright SW, Van den Enden RL, Pearce I, Davidson AT, Scott FJ, et al. 2010. Phytoplankton community structure and stocks in the Southern Ocean (30–80° E) determined by CHEMTAX analysis of HPLC pigment signatures. *Deep-Sea Res Pt I* **57**: 758–778.

Yager PL, Sherrell RM, Stammerjohn SE, Alderkamp A-C, Schofield O, et al. 2012. ASPIRE: The Amundsen Sea Polynya International Research Expedition. *Oceanography* **25**(3): 30–43.

Yager PL, Wallace DWR, Johnson KM, Smith Jr WO, Minnett PJ, et al. 1995. The Northeast Water Polynya as an atmospheric CO_2 sink: A seasonal rectification hypothesis. *J Geophys Res* **100**: 4389–4398.

Contributions

- Contributed to conception and design: PLY, RMS, SES, HWD, OMES, LR, SB, ACA
- Contributed to acquisition of data: PLY, RMS, SES, HWD, OMES, EDI, SEW, KEL, ACA, JD, RL, IR, RES, RGN, AFP, RS, GLvD
- Contributed to analysis and interpretation of data: PLY, RMS, SES, HWD, OMES, EDI, SEW, KEL, CMW, ACA, JD, RL, AJM, LM, RGN, RS, GLvD
- Drafted and or revised the article: PLY, RMS, SES, HWD, KEL, JD, RS.
- Approved the submitted version for publication: PLY, RMS, SES, HWD, OMES, EDI, SEW, KEL, CMW, LR, SB, ACA, JD, RL, IR, RES, AJM, LM, RGN, AFP, RS, GLvD.

Acknowledgments

We thank Captain Y. Maghrabi, the crew of the RV *Nathaniel B. Palmer,* MPC E. Hutt, and the rest of the Raytheon Polar Services Company (RPSC) support team for their hard work, dedication, and team effort. L. Ekern (RPSC) performed the nutrient analysis onboard. S. Kjellerup contributed to mesozooplankton collection. Thanks also to the rest of the ASPIRE scientists onboard for the great team effort, and to the Yager Lab group for providing many useful comments and feedback, especially K. Sines, T. Connelly, B. Page, and H. Oliver. A special thanks to L. Schoeller, M. LaRue, and P. Morin at the AGIC for providing ASPIRE with near real-time MODIS Terra images at sea, and to E.P. Abrahamsson (British Antarctic Survey) for generating the original polynya cruise track map on the January 1 MODIS image (Figure 1). TG Nielsen provided support to some of the team. *Oden Southern Ocean*, SWEDARP 2010/11, was organized by the Swedish Polar Research Secretariat and National Science Foundation Office of Polar Programs. We appreciated the cooperation and support of IB *Oden* Captain M. Peterson, as well as that of the co-chief scientists onboard *Oden*, R. Dickhut and K. Abrahamsson. Very special thanks to R.R. Marinelli and S.M. Holland for making this effort possible.

Funding information

This project was funded by NSF Office of Polar Programs, Antarctic Organisms and Ecosystems (ANT-0839069 to PY, ANT-0838995 to RMS, ANT-0838975 to SS, ANT-0839012 to HWD, and ANT-0944727 to K Arrigo for support of ACA, GLvD and KEL). We also acknowledge support for participation of AFP by NSF (ANT-08-39012 to HWD and ANT 15-42220 to AFP) and for Swedish collaborators from the Swedish Research Council (#2008-6430 to S. Bertilsson and L. Riemann, and #2008-6429 to P.-O. Moksness and J. Havenhand, which supported participation of RS and SK).

Competing interests
The authors have no competing interests or conflicts of interest.

Data accessibility statement
All data will be publically available from BCO-DMO: http://www.bco-dmo.org/project/2132.